High Power Continuous Wave Laser Heating and Damage with Contamination, and Non-Uniform Spectrally Dependent Thermal Photon Statistics

A Dissertation
SUBMITTED TO THE FACULTY OF
UNIVERSITY OF MINNESOTA
BY

Kyle David Olson

IN PARTIAL FULFILLMENT OF THE REQUIREMENTS
FOR THE DEGREE OF
DOCTOR OF PHILOSOPHY

Joseph John Talghader

December 2015

Acknowledgements

This dissertation was made possible by many people and organizations. I would like to thank my advisor Dr. Joey Talghader for supporting and guiding me in my graduate career. My colleagues Andrew Brown, and Luke Taylor contributed significantly to this research and their efforts are greatly appreciated. This research was founded by a number of different agencies including Initiative for Renewable Energy and the Environment, 3M, the Joint Technology Office, Army Research Office, Penn State Electro-Optics Center, the University of Minnesota and is greatly acknowledged.

I would also like to acknowledge both my past and present colleagues Nick Gabriel, Anand Gawarikar, Ryan Shea, Sangho Kim, Wing Chan, Merlin Mah, Philip Armstrong, Jon Lake, Yu-Jen Lee, Tirtha Mitra, Jordan Burch, Brad Tiffany, Sara Rothwell, Joe Stansbery, Ethan Torrey, and Di Lin for their help over the years. I would also like to thank the staff at the Minnesota Nano Center, and the Characterization Facility at the University of Minnesota for their help in fabrication and characterization of devices.

Finally I would like to acknowledge my friends and family especially Mary Kay Marino for her undivided support, Charlie Spanjers and Brad Guertin for their unconditional friendship, and my parents Mary and Robert Olson for their support.

Abstract

A model is presented and confirmed experimentally that explains the anomalous behavior observed in the continuous wave (CW) excitation of thermally-isolated optics. Very low absorption, high reflective optical thin film coatings of HfO_2 and SiO_2 were prepared. When illuminated with a laser for 30s the coatings survived peak irradiances of 13MW/cm^2. The temperature profile of the optical surfaces was measured using a calibrated thermal imaging camera; about the same peak temperatures were recorded regardless of spot size, which ranged between 500μm and 5mm. This phenomenon is explained by solving the heat diffusion equation for an optic of finite dimensions, including the non-idealities of the measurement. An analytical result is also derived showing the transition from millisecond pulses to CW, where the heating is proportional to the laser irradiance (W/m^2) for millisecond pulses, and proportional to the beam radius (W/m) for CW.

Contamination-induced laser breakdown is often viewed as random and simple physical models are difficult to apply. Under continuous wave illumination conditions, failure appears to be induced by a runaway free-carrier absorption process. High power laser illumination is absorbed by the contaminant particles or regions, which heat rapidly. Some of this heat transfers to the substrate, raising its temperature towards that of the vaporizing particle. This generates free carriers, causing more absorption and more heating. If a certain threshold concentration is created, the process becomes unstable, thermally

heating the material to catastrophic breakdown. Contamination-induced breakdown is exponentially bandgap dependent, and this prediction is borne out in experimental data from TiO_2, Ta_2O_5, HfO_2, Al_2O_3, and SiO_2.

The spectral dependence of blackbody radiation and thermal photon noise is derived analytically for the first time as a function of spectra and mode density. An algorithm by which the analytical expression for the variance can be found for any spectral distribution is also presented. The analytical results of some simple distributions are found and shown to be inaccurately approximated with a uniform spectral distribution highlighting the importance of the finding. Two microcavities are then presented to exemplify enhanced or inhibited photon statistics effects on the cavity.

Table of Contents

List of Tables

List of Figures

Chapter 1

Introduction

1.1 Thesis Organization

This thesis is organized into three sections. The first two sections deal with CW laser heating of low absorption and contaminated optics and the theoretical process of breakdown. The following section delves into the mathematical explanation of spectrally dependent thermal photon noise.

Chapter 2 will describe the mathematical treatment of CW laser heating from short millisecond pulses to infinite time steady state solutions and all time in between. The results are compared to experiments with low absorption optical mirrors with multiple materials in both the film and substrates.

Chapter 3 takes the solutions from Chapter 2 a step further to include time varying laser power and absorption, allowing for simulations of contaminated optics. The results obtained are then manipulated to find physical evidence of a predictable method of contamination-induced breakdown of optics under CW illumination. The results are then compared with and borne out by experiments.

Chapter 4 describes the problem of thermal photon noise and its spectral dependence. An algorithm is presented in order to calculate from fundamental thermodynamics the spectral dependence of thermal photon statistics. The spectral dependence of a few simple spectrums are analyzed and solved for analytically.

1.2 Laser Heating and Damage

The study of laser interactions with materials has primarily developed using ultra-short pulsed lasers [1–4]. However, many applications of laser heating involve continuous wave (CW) lasers [5–8], and their corresponding thermal material damage mechanisms are poorly understood. In previous research, there have been seeming anomalies in the temperature distributions seen under CW excitation [5,8,9]. In this paper, a model for high power CW heating of very low absorption mirrors is developed and tested that explains these anomalies.

Solutions to the steady state laser heating problem was developed throughout the 1970's and 80's [8,10–12]. This work modeled nonlinear absorption, reflection, density, specific heat, and thermal conductivity [8,11]. Expanding these derivations to include thermal loading into a single equation covering the time scale from millisecond pulses to

steady state solutions is desired. The general relationship between incident power, material properties, and duration of pulse as they affect the temperature rise of an optic are also interesting properties that could be gathered from a general solution to the laser heating problem.

The temperature rise of contaminated optics could play an important role in the breakdown of optics in non-laboratory environments where failurae occurs at laser intensities many orders of magnitude lower than predicted by the fundamental materials limits probed by ultra-short pulse lasers [13,14]. The difference is often attributed to environmental contamination [14,15], which to date has been considered a random process better explored by statistical techniques than theoretical physics. However, given the scientific and economic importance of high power lasers in medical, industrial, and military applications, a cogent physical theory of contamination-induced optical breakdown would have an immediate impact on optical materials selection, coating design, and laser system design.

It is well known that multiphoton absorption and impact ionization initiate ultra-short pulse laser breakdown [1,2,16–20]. These are both field-mediated phenomena with significant bandgap dependences. For continuous wave (CW) lasers, breakdown is often a purely thermal process, so low absorption materials are favored. Popular choices for materials have been oxides, specifically Alumina (Al_2O_3), Hafnia (HfO_2), Silica (SiO_2), Tantala (Ta_2O_5), and Titania (TiO_2). All of these materials, when in a pristine state with no contamination, can withstand exceptionally high CW irradiances and have Laser

Damage Thresholds (LDT) above 3MW/cm^2. However, it has been noted that once contaminated, the damage characteristics of these oxides become significantly different.

The differences in contamination-induced laser damage thresholds could be explained by thermally generated free carrier absorption. Contaminant regions absorb laser light and begin to vaporize. Some of this heat is transferred to the immediately underlying substrate, whose local temperature rises toward that of the contaminant. This generates free carriers. Once a threshold value for the generated free-carrier density is reached, absorption due to free carriers begins to heat the substrate independently of the contaminant, and the free carrier generation and absorption process spirals to catastrophic failure.

1.3 Thermal Photon Noise

Thermal photons are everywhere. Everything that has a non-zero temperature emits thermal photons at a rate first proposed by Max Planck in 1900 and defined by Planck's law [21]. In deriving Planck's law photons are assumed to follow a Boltzmann distribution and to be quantized. Because Planck's law can accurately describe the spectral distribution of light intensity emitted from a black body, using the same assumptions for calculating the thermal photon noise should hold.

Detecting and sensing thermal photons has many practical applications in medical, military, chemistry, astronomy, and many more industrial disciplines. Understanding the noise in thermal sources can drastically effect the design and fabrication of devices to improve performance and drive further innovations. Today more

and more applications are being developed with smaller and smaller features. These micro-devices provide new challenges when studying thermal photon noise mainly because of the limited number of allowed optical modes within the device.

Micro-cavity emitters and detectors in addition to having a limited number of modes, can also have spectrally dependent modal distributions. Non-uniform modal distributions can arise from cavity design (e.g. Fabry-Pérot), light intensity (e.g. spectral hole burning), and many other causes. The thermal photon noise calculated for blackbody sources is considered in the literature only for a square or uniform spectral dependence or for infinite modes, and has not received significant attention since the 1950's [22–25]. With recent advancements in micro fabrication, thermal detection devices have become small enough to warrant a study of systems with small numbers of modes and non-spectrally uniform mode distributions [22,26,27].

This thesis will explore the mathematical approach of calculating thermal photon noise and introduce a new method containing the spectral dependence of the modal distribution.

Chapter 2

Continuous Wave Laser Heating

Much of this chapter was taken from an already published work by the author [28]. Most laser heating and damage tests in the past have concentrated on pulsed lasers where irradiances are extremely high, and the time scale is extremely short. When the theories to describe phenomena in the pulsed regime are translated to Continuous Wave (CW) lasers, many results are not reproducible. Some irregularities in the CW regime include catastrophic failure that cannot possibly be produced by the relatively low intensities of CW lasers, yet the optics still fail, in a statistical manner however. In the pulsed regime optics usually have a well-defined LDT usually quoted as an energy density in units of J/cm^2. Whereas in the CW case optics rarely fail consistently and the LDT is quoted as a

power density in units of W/cm^2, but even then things like spot size and duration of pulse could change the LDT observed in experiment.

One reason for these irregularities is our relatively poor understanding of the thermodynamics at play during a CW laser shot versus a pulsed laser. Unfortunately the thermal diffusion equations do not have analytical solutions to the CW laser heating problem whereas there are plenty of ways of analyzing the pulsed regime analytically. Because of this poor understanding one might expect the temperature rise of an optic under CW illumination to be determined by the laser intensity, but as seen later in Figure 2.4, it is not.

Analytical approaches were needed to describe CW laser heating and are presented here for the first time for some limiting cases. These analytical techniques will clarify some of the seemingly anomalistic behavior seen during CW laser shots.

2.1 Heat Equation Solution with Heat Generation Term

The motivation for the following derivation was that a simple and fast 3D numerical model was not available for CW laser illumination on high reflectivity optics. Many of the simple numerical models required time steps that were too short to retain stability and simulate for more than a few milliseconds. In general the solution to the laser heating problem comes from solving the partial differential heat equation with linear thermal properties.

$$\frac{\partial T}{\partial t} = \alpha \nabla^2 T + \frac{q(r,z,t)}{\rho c} \tag{2.1.1}$$

T is the temperature profile in cylindrical coordinates. The laser beam can be assumed to be cylindrically symmetric, eliminating the angular dependence. Furthermore, α is the thermal diffusivity, $q(r,z,t)$ is the generated heat term, ρ is the density, and *c* is the specific heat. To solve this equation we first solve for a uniform energy pulse in radius and a delta function in depth (*z*) and time (*t*). This solution is readily available and is given below for the boundary conditions $T|_{z=\infty} = T_0$ and $dT/dz|_{z=0} = 0$ [29,30].

$$T(z,t) = T_0 + \frac{E/A}{\rho c\sqrt{\pi\alpha t}} e^{\left(\frac{-z^2}{4\alpha t}\right)}$$
$$\frac{\Delta T(z,t)}{\Delta T_C} = \frac{T(z,t) - T_0}{\Delta T_C} = \frac{1}{\sqrt{\pi\alpha t}} e^{\left(\frac{-z^2}{4\alpha t}\right)} \quad (2.1.2)$$

Here $\Delta T_C = E/(A\rho c)$ and is the characteristic temperature scale where E/A is the total energy per unit area delivered in the pulse. In this solution it is also assumed that the total energy of the pulse exists in the semi-infinite domain $0 \leq z \leq \infty$ at all times. Next we solve for the dissipation of a Gaussian temperature profile in a one dimensional cylinder. We can solve this problem using separation of variables and Fourier analysis to get the following well-known result [29,30]:

$$\frac{\Delta T(r,t)}{\Delta T_C} = \frac{1}{2\pi w(t)^2} e^{\left(\frac{-r^2}{2w(t)^2}\right)}$$
$$w(t)^2 = w^2 + 2\alpha t \quad (2.1.3)$$

Now $\Delta T_C = E/(L\rho c)$, w is half of the laser pulse beam width, and $w(t)$ represents how the temperature profile width changes over time assuming a 2D Gaussian laser profile.

We can find the 3D solution to the heat equation for an infinitely fast Gaussian laser pulse that is completely absorbed at the surface ($z = 0$) by combining the two solutions of equations (2.1.2) and (2.1.3) using product solution. In the final solution $\Delta T_C = E/\rho c$ and is used to convert the diffusion profiles to temperature from the energy input to the system.

$$\Delta T(r,z,t) = \frac{E}{2\pi^{3/2}\rho c\sqrt{\alpha}} \frac{e^{\left(\frac{-r^2}{2w^2+4\alpha t}\right)} e^{\left(\frac{-z^2}{4\alpha t}\right)}}{\sqrt{t}(w^2+2\alpha t)} \tag{2.1.4}$$

Where E is the total energy of the laser pulse. Equation (2.1.4) gives a very nice analytical expression for the diffusion of a Gaussian energy pulse but it is not valid for a continuous wave (CW) laser where the pulse duration is long enough that the temperature can diffuse while the laser is still on. In the past the heat equation (2.1.1) has been solved for very long duration pulses ($t = \infty$) and very short pulses ($t \ll w^2/2\alpha$) [7,9–12] whereas we provide a solution for all times. A first simplification is that in a small increment of time, the energy can be replaced with a power multiplied by time. This power is the fraction of the power of the laser multiplied by the absorption of the surface.

$$E = \eta P_{Laser}\Delta t = P_{absorbed}\Delta t \tag{2.1.5}$$

Where η is the fraction of laser power that is absorbed at the surface and Δt is the duration of the pulse. Now plugging (2.1.5) into (2.1.4) and taking the limit where Δt goes to dt and integrating over the duration of the pulse we get an expression for the time-dependent heating of a CW laser.

$$\Delta T(r,z,t) = \frac{P_{absorbed}}{2\pi^{3/2}\rho c\sqrt{\alpha}} \int_0^t \frac{e^{\left(\frac{-r^2}{2w^2+4\alpha t\prime}\right)} e^{\left(\frac{-z^2}{4\alpha t\prime}\right)}}{\sqrt{t'}(w^2+2\alpha t')} dt\,' \tag{2.1.6}$$

Where, t, is the total time the CW laser power is applied to the optical surface. Equation (2.1.6) integrates over all the infinitesimally short pulses and allows them to diffuse for t' seconds. At the point where *r* is zero the maximum power of the laser is incident on the surface $(z = 0)$, it is this point where material changes and damage will most likely first occur. To solve this equation analytically we can take *r* to be zero and *t* to be infinite to get the *z* dependence at steady state, or *r* and *z* to be *0* to get the time dependence at the location of maximum temperature. The point of maximum temperature is of particular interest in laser damage testing as it is likely the location of damage initiation.

$$\Delta T(0,z,\infty) = \frac{P_{absorbed}}{kw2\sqrt{2\pi}} e^{\left(\frac{z^2}{2w^2}\right)} \mathrm{erfc}\left(\frac{|z|}{w\sqrt{2}}\right) \tag{2.1.7}$$

$$\Delta T(0,0,t) = \frac{P_{absorbed}}{kw\pi\sqrt{2\pi}} \tan^{-1}\left(\frac{\sqrt{2\alpha t}}{w}\right) \tag{2.1.8}$$

Where erfc(*x*) is the complimentary error function and is defined as the integral of the Gaussian distribution from *x* to ∞ with a leading factor of $2/\sqrt{\pi}$, and k is the thermal conductivity. Note that $\alpha = k/c\rho$. Notice that if $t \ll w^2/2\alpha$ signifying a short pulse, then the $\tan^{-1}$ can be approximated by the small angle theorem and gives the following.

$$\Delta T(0,0,t) \cong \frac{P_{absorbed}}{w^2} \frac{\sqrt{\alpha t}}{k\pi^{3/2}} \tag{2.1.9}$$

We can also simplify equation (2.1.8) for long duration pulses where ($t = \infty$), and $\tan^{-1}$ reduces to $\pi/2$.

$$\Delta T(0,0,\infty) = \Delta T_{max} = \frac{P_{absorbed}}{w}\frac{1}{k2\sqrt{2\pi}} \tag{2.1.10}$$

Equations (2.1.9) and (2.1.10) agree with previous publications [7,10–12] and show that for short duration pulses the temperature rise is dependent on irradiance and scales as the inverse of the beam area ($1/m^2$), and for longer pulses scales as the inverse of the beam radius (1/m). Equation (2.1.8) defines how the system behaves at all times. The time when equation (2.1.9) becomes invalid can be found by using the small angle approximation of $\tan^{-1}$, to at least 1% accuracy we require the condition:

$$t < 0.01527\frac{w^2}{\alpha} \tag{2.1.11}$$

For SiO_2 with a laser beam radius of w = 0.5mm, the condition is $t < 5ms$. This shows that for CW laser heating of low absorption optics the temperature rise does not depend on the irradiance of the laser (W/m^2) but on the inverse of the laser beam radius (W/m). To approximate the $\tan^{-1}$ function to 1% accuracy for large angles requires that:

$$t > 2026.1\frac{w^2}{\alpha} \tag{2.1.12}$$

Another important solution to the laser heating problem is cooling by self-quenching, where the bulk material is a heat sink, after the laser is off. To find this solution without taking into account any convective losses we need to integrate equation (2.1.6) from t to $t + t_p$ where t_p is the duration of the pulse.

$$\Delta T(r,z,t) = \frac{P_{absorbed}}{2\pi^{3/2}\rho c\sqrt{\alpha}} \int_{t}^{t+t_p} \frac{e^{\left(\frac{-r^2}{2w^2+4\alpha t'}\right)} e^{\left(\frac{-z^2}{4\alpha t'}\right)}}{\sqrt{t'}(w^2+2\alpha t')} dt' \qquad (2.1.13)$$

Equation (2.1.13) integrates over all the infinitesimally small pulses but allows each pulse to diffuse for an extra amount of time t. If we take the limit as $t \to 0$ then we recover equation (2.1.6). To solve equation (2.1.13) analytically we take *r* and *z* to be 0 and get the result below. We have also replaced t with $t - t_p$ and enforced the rule $t \geq t_p$ to give real results.

$$\Delta T(0,0,t) = \frac{P_{absorbed}}{kw\pi\sqrt{2\pi}} \left(\tan^{-1}\left(\frac{w}{\sqrt{2\alpha(t-t_p)}}\right) - \tan^{-1}\left(\frac{w}{\sqrt{2\alpha t}}\right)\right) \qquad (2.1.14)$$

2.2 Experiment

We confirmed our model experimentally by measuring the surface temperature of an ultra-low absorbing optical thin film which was exposed to high power CW laser light. High reflectivity is desired in the thin film to limit substrate absorption. For this reason high reflectivity Distributed Bragg Reflectors (DBR) were designed and fabricated using ion-beam sputtering by Advanced Thin Films. We measured the optical surface absorption using Photothermal Common-Path Interferometry (PCI) and observed an average absorption of 7ppm for HfO_2/SiO_2 high reflectivity DBR's and less than 1ppm for Ta_2O_5/SiO_2 DBRs. The DBRs were tuned to have a peak reflectivity at a wavelength of 1.064μm. The laser was a 17kW CW Ytterbium doped IPG photonics YLS-1700 laser outputting at 1.070μm at the Electro Optics Center (EOC) at Penn State. The laser is

capable of emitting 0.880kW to 15.5kW reliably and can focus to a spot size ranging from 0.5mm to 7.2mm, resulting in an irradiance range of 6.32×10^{-4} to 13.3MW/cm^2.

The optic being tested was slightly misaligned so that the beam is reflected back to an absorbing carbon block as seen in Figure 2.1. If the optical coating fails, the laser propagates through the optic into an integrating sphere automatically shutting down the laser.

Prior to testing each optic, both surfaces were cleaned on the front and back sides by drag wiping with a lens tissue using a drop of methanol as the solvent. The tissue was only used once, and up to three drag wipes were performed on each side of the optic to be tested.

In cases where the optics did not fail, the spatial surface temperature distribution was measured using an infrared camera capable of measuring a temperature range from 0 to 250°C at a 30Hz frame rate. The optics were placed on a motorized XY stage to automate testing. The optics under test were super-polished SiO_2 optical flats, 1 inch in diameter and 0.25 inches thick, or 1 inch Si wafers. The substrates were coated with HfO_2/SiO_2 or Ta_2O_5/SiO_2 DBR coatings. Because the Ta_2O_5/SiO_2 DBRs had extremely low absorption properties (< 1 ppm), the camera could not reliably measure the temperature rise during a laser shot, so the data presented here concentrates on the HfO_2/SiO_2 coatings. In Figure 2.1 the experimental setup of the laser and beam path is shown.

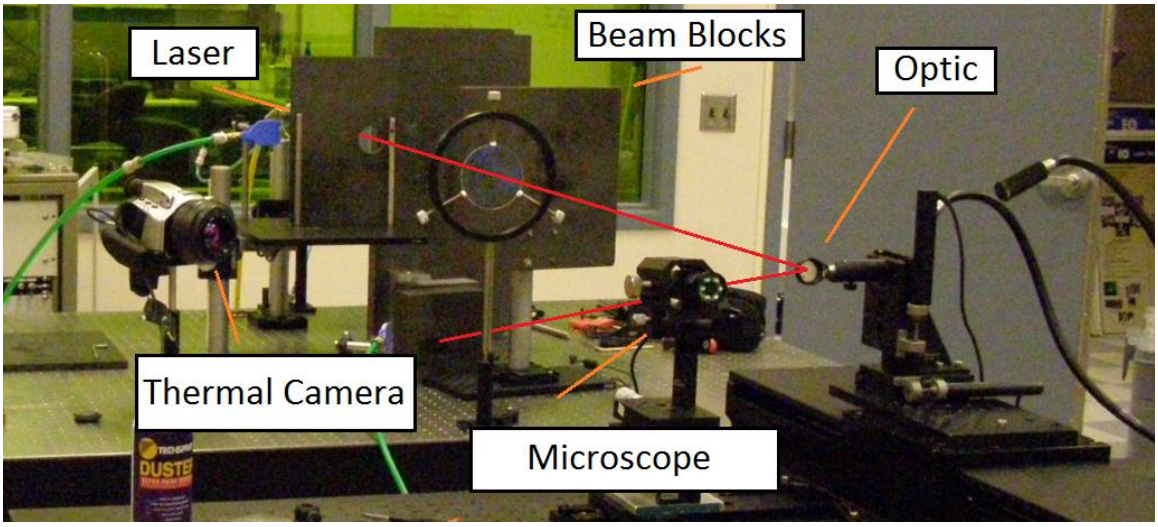

Figure 2.1 Experimental Setup with beam path added for clarity. The reflective optic is slightly misaligned to send the reflected beam to an absorbing carbon block.

Each individual optic was tested either to avoid laser conditioning (the slow strengthening of an optical element by exposing it to gradually increasing intensities of laser light) or to intentionally condition the optic. There were 9 testing sites on each optic; at the first site, 10 shots were completed in succession to condition the optic. As we moved through the sites fewer successive shots were performed (to vary the level of conditioning) until at the 9^{th} site, only the highest power density was used. In Figure 2.2 the experimental maximum change in temperature versus time is compared with the analytical result of equation (2.1.8). The shot showing a lower thermal rise was conditioned with one extra shot at 70% power, reducing the average absorption by 12.9%, to get the right fit with all other parameter remaining the same, from 7ppm to 6.1ppm. The drop in absorption was not able to be confirmed by PCI measurements so we cannot be certain that this change was from conditioning. The thermal properties used in the analytical result were a volumetric average of the materials within the film.

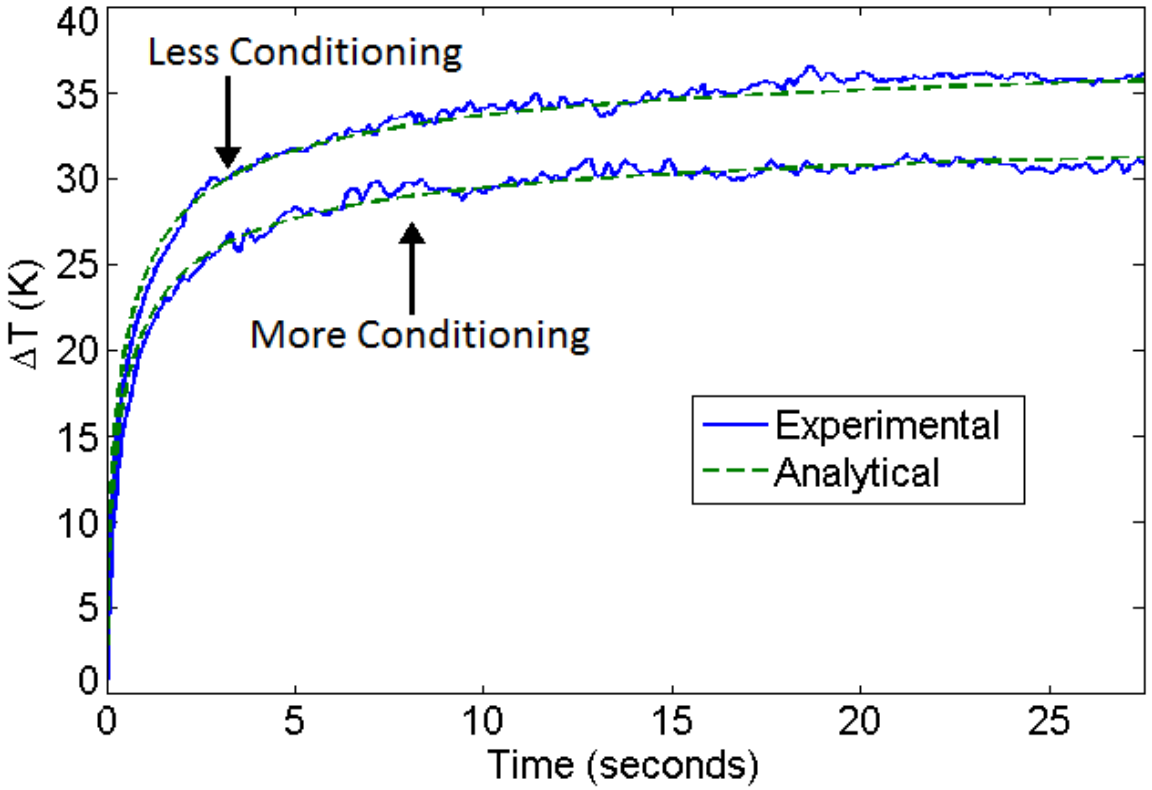

Figure 2.2 Laser heating of SiO_2 1 inch optical flat with HR HfO_2/SiO_2 DBR coating. P_{laser} = 15.5[kW], w = .55[mm], c = 522[J/(kg·K)], ρ = 5710[kg/m^3], k = 1.02[W/(m·K)], α = 3.43x10^{-7}[m^2/s]. The thermal properties are an average of the materials within the film.

We were also able to test multiple laser spot sizes at different locations on the optic. In Figure 2.3 we show how the analytical result fits with varying spot sizes. Notice that although the larger spot size produces less heating the model shows that there is more absorption. In the next section we discus non-ideal conditions and see if the absorption results in Figure 2.3 were real or due to other effects.

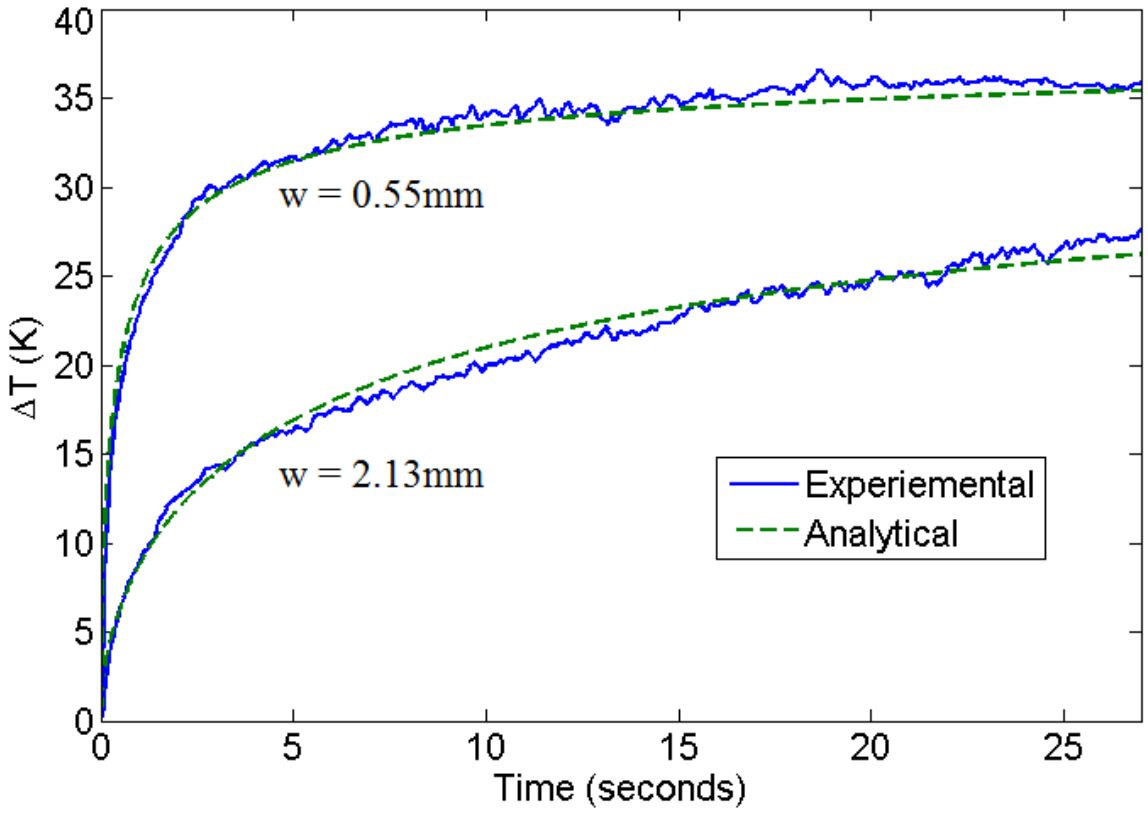

Figure 2.3 Laser heating comparison of differing spot sizes. For (*w* = 0.55mm) absorption = 14ppm, and (*w* = 2.13mm) absorption = 26ppm.

From testing multiple spot sizes another relationship of temperature rise and intensity was obtained. The expected relationship was that the temperature rise would be proportional to the power density of the laser but that is not what was recorded as seen in the following Figure 2.4. Instead independent of spot size it appears that the total power of the laser more significantly affects the maximum temperature.

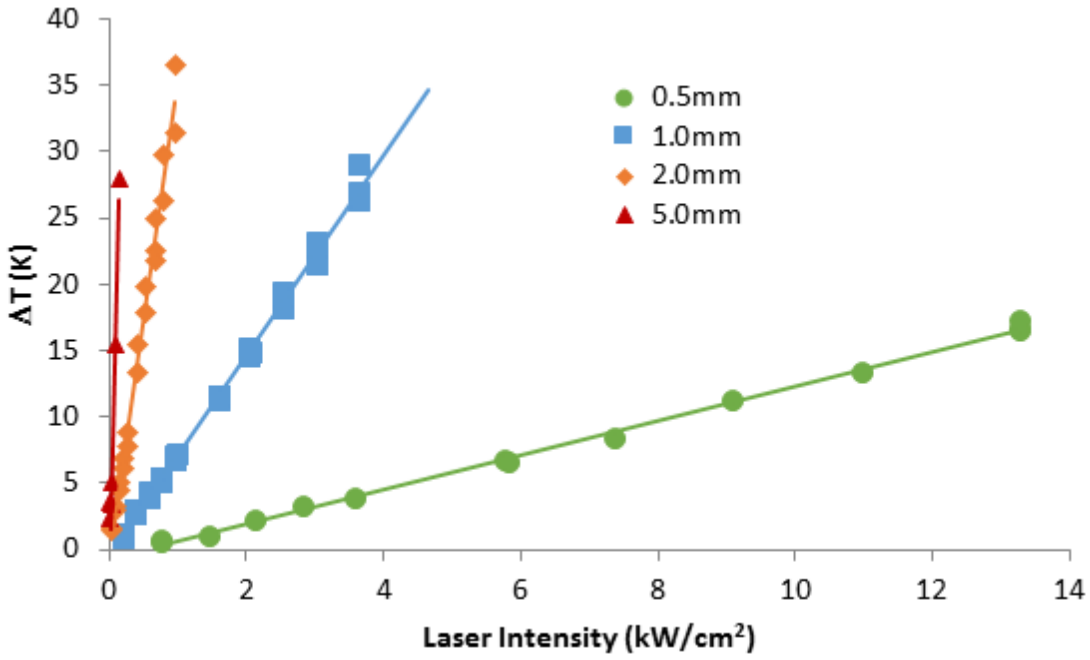

Figure 2.4 Temperature rise as a function of laser intensity for different spot sizes on HfO_2/SiO_2 DBR mirrors, from steepest to shallowest slope the spot size is 5, 2.0, 1.0, and 0.5mm.

2.3 Non-Ideal Effects

The data closely followed the model as shown, but there are a few experimental non-idealities we would like to address. First, the optic under laser illumination is neither infinite in radius nor semi-infinite in z, second, the resolution of the thermal camera is not infinite, and, third, the optic has additional thermal losses besides diffusion. Constraining the diffusion to finite dimensions requires the use of an insulating boundary condition. Without defining these boundary conditions we can solve the problem by using the result from the infinite case. An insulating boundary condition can be thought of a reflecting boundary condition where the heat that would diffuse through the boundary is instead reflected, insuring a zero slope at the boundary. By taking the infinite result and summing

duplicates offset by twice the distance to the boundary produces this reflecting case and also satisfies the insulating boundary conditions [29,30].

$$\Delta T(z,t) = \frac{E/A}{\rho c L}\vartheta_3\left(\frac{\pi z}{2L}, e^{\left(\frac{-\pi^2 t\alpha}{L^2}\right)}\right)$$
$$\Delta T(z=0,t) = \frac{E/A}{\rho c\sqrt{\pi\alpha t}}\vartheta_3\left(0, e^{\left(\frac{-L^2}{\alpha t}\right)}\right) \quad (2.3.1)$$

$$\Delta T(r,t) = \frac{\frac{E}{L}\vartheta_3\left(\frac{\pi r}{2R}, e^{\left(\frac{-\pi^2(w^2+2\alpha t)}{2R^2}\right)}\right)}{\rho c 2R\sqrt{2\pi(w^2+2\alpha t)}}$$
$$\Delta T(r=0,t) = \frac{\frac{E}{L}\vartheta_3\left(0, e^{\left(\frac{-2R^2}{w^2+2\alpha t}\right)}\right)}{\rho c 2\pi(w^2+2\alpha t)} \quad (2.3.2)$$

In the previous equations ϑ_3 is the Jacobi Theta function of the third kind and is essentially an infinite sum of exponential functions each offset from each other by either 2L or 2R. Combining equations (2.3.1) and (2.3.2) and integrating over time we get a new expression for the laser heating response.

$$\Delta T(r=0,z=0,t) = \frac{P_{absorbed}}{2\pi^{3/2}\rho c\sqrt{\alpha}}\int_0^t \frac{\vartheta_3\left(0, e^{\left(\frac{-L^2}{\alpha t}\right)}\right)\vartheta_3\left(0, e^{\left(\frac{-2R^2}{w^2+2\alpha t}\right)}\right)}{\sqrt{t'}(w^2+2\alpha t')}dt' \quad (2.3.3)$$

This equation no longer has an analytical result, and does not converge to a finite temperature as $t \to \infty$. However equation (2.3.3) more accurately depicts CW laser heating when solved numerically compared to equation (2.1.6) when L is small compared to the diffusion length $\sqrt{\alpha t}$ or R is small compared to Gaussian width ($w^2 + 2\alpha t'$). It is also

important to note that equation (2.3.3) will most likely be needed to model the situation where a suspended film is being illuminated by laser light.

Suspended films should have a lower LDT because of the relatively rapid (nanoseconds) heating of the surface, which diffuses almost instantaneously to the other side of the film. Once this happens there is nowhere for the heat to go and the film will indefinitely heat up until damage or another thermal loss mechanism takes over, such as radiation or conduction through the suspended film supports. We were able to see a similar situation by illuminating films deposited on 1 inch diameter and 0.5mm thick silicon wafers. The Si wafer has about 2 orders of magnitude higher thermal conductivity than glass substrates and is much thinner allowing the heat to dissipate to the back side of the optic.

We show in Figure 2.5 both experimentally and theoretically that a finite R and L can greatly change the temperature response at the surface compared to the analytical result of equation (2.1.8). The two experimental results are measurements of the same optic under the same laser illumination and conditioning state, but at different locations on the optic. Still the only fitting parameter is the absorption at the surface, and we found that on Si the films were 2 to 3 times more absorptive. The absorption of these films could not be directly measured with PCI due the interfering effects of the absorptive Si substrate.

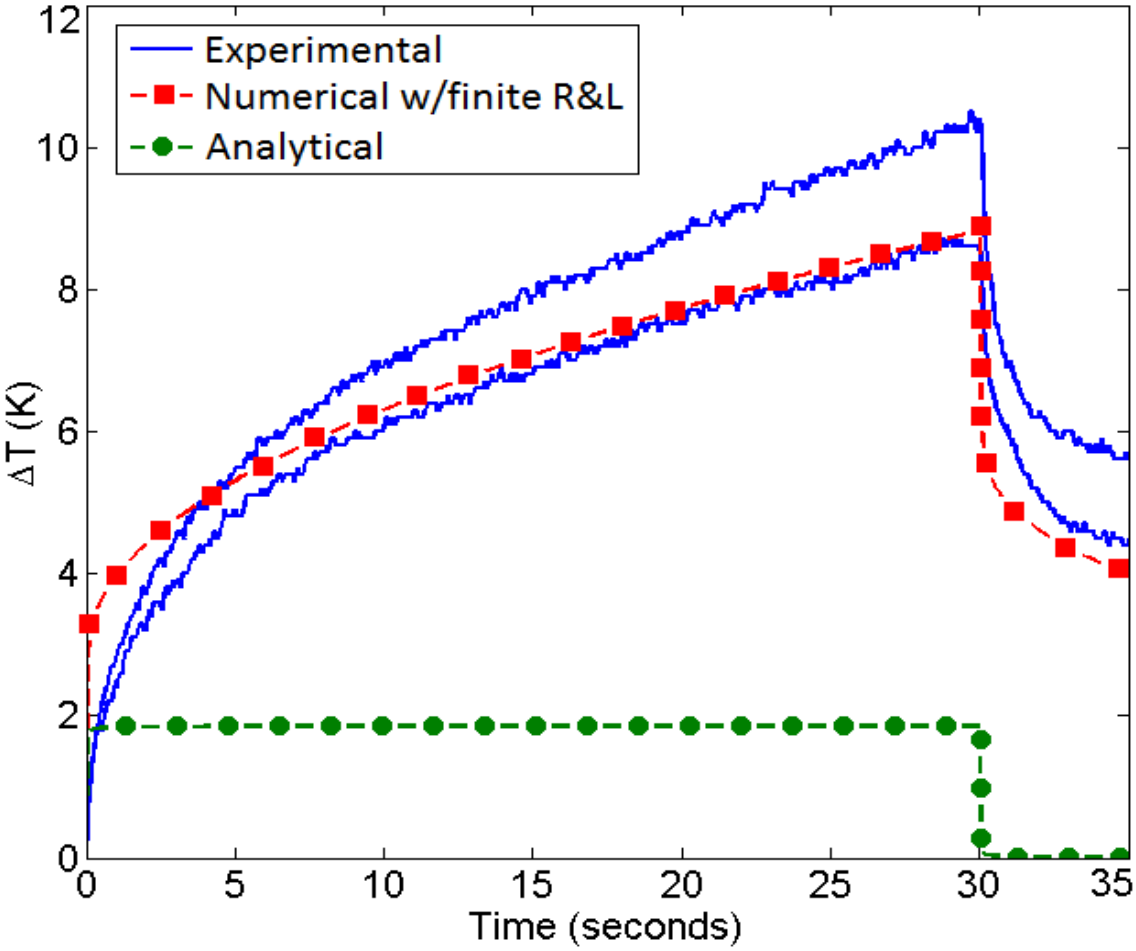

Figure 2.5 Laser heating of Si wafer with HR HfO_2/SiO_2 DBR coating. The two experimental lines are 2 different laser shots of the same power level at different spots on the sample. P_{laser} = 15.3[kW], absorption = 25[ppm], w = .275[mm], c = 705[J/(kg·K)], ρ = 2329[kg/m^3], k = 149[W/(m·K)], α = 9.07x10^{-5}[m^2/s], R=12.7[mm], L=0.5[mm]. The analytical curve shows the prediction for a semi-infinite optic (i.e. one with low thermal conductivity as in equations (2.1.8) and (2.1.14) and Figures 2.2 and 2.3.)

In Figure 2.5 we use the substrate material parameters in the model rather than a volumetric average of the film as in Figure 2.2 and 2.3. Previously the substrate was similar to the film and the thermal conductivity was low so that much of the thermal energy existed in the film and near the surface, now with a higher thermal conductivity in the substrate more of the thermal energy exists within the substrate and thus we use the substrate material parameters. At shorter illumination times, from Figure 2.5, it appears that the experiment

showed less heating than expected and at longer illumination times it matches the calculations. This could be because we have not taken into account the much lower thermal conductivity of the surface film absorbing the laser at short times, and at larger times the heat is sufficiently diffused into the Si substrate so that the experiment is closer to the modeled case. It appears that the surface is also losing heat more slowly than expected from the model. The maximum temperature change is much lower on Si substrates than on SiO_2 substrates but equation (2.3.3) predicts that the absorption is actually higher for the films on Si substrates. The higher absorption values are likely due to light leakage through the high reflective coating into the substrate. The DBR transmission is approximately 10 to 20ppm with the remaining power absorbed in the substrate causing the increase in absorption.

To take into account the resolution of the thermal camera we can average equation (2.3.2) over the field of view of a pixel located at the center of the laser beam. Noticing $r^2 = x^2 + y^2$ we can easily average over a square pixel area. We also assume that $R \gg (w^2 + 2\alpha t)$ so that the Jacobi Theta function reduces back to a Gaussian.

$$\frac{1}{Area}\iint\limits_{Square} e^{\left(\frac{-r^2}{2w^2+4\alpha t}\right)} r dr d\theta = \frac{1}{P_s^2}\iint_{-P_s/2}^{P_s/2} e^{\left(\frac{-x^2-y^2}{2w^2+4\alpha t}\right)} dx dy$$
$$= \frac{2\pi(w^2+2\alpha t)}{P_s^2}\,\mathrm{erf}\left(\frac{P_s}{2\sqrt{2(w^2+2\alpha t)}}\right)^2 \tag{2.3.4}$$

In equation (2.3.4) P_s is the length of the side of a pixel in the thermal camera. Substituting equation (2.3.4) into (2.3.3) we'll get our final model for laser heating.

$$\Delta T(r=0,z,t) = \frac{P_{absorbed}}{P_s^2 \rho c \sqrt{\pi\alpha}} \times \int_0^t \frac{\vartheta_3\left(0, e^{\left(\frac{-L^2}{\alpha t}\right)}\right)\vartheta_3\left(0, e^{\left(\frac{-2R^2}{w^2+2\alpha t}\right)}\right)}{\sqrt{t'}} \operatorname{erf}\left(\frac{P_s}{2\sqrt{2(w^2+2\alpha t')}}\right)^2 dt' \quad (2.3.5)$$

With equation (2.3.5) we can explain why experiments at spot sizes below the pixel resolution did not show an increase in the maximum temperature reading with decreasing spot size. With a spot size of w = 0.15mm and a laser power of 15.5kW (an 8 times higher irradiance than that of the shots in Figure 2.2, with the same optic) a temperature rise of about 17K was seen. The thermal camera in this experiment was placed sufficiently far enough away to produce a resolution of P_s = 2mm which is much larger than the laser spot size. From this data we can see in Figure 2.6 that the actual temperature rise of the optic was probably around 85K, about 5 times hotter than recorded by the thermal camera in all 3 successive shots. The 3 experimental results shown in Figure 2.6 are laser shots on the same optic and at the same laser power with different pulse durations at 3 different locations.

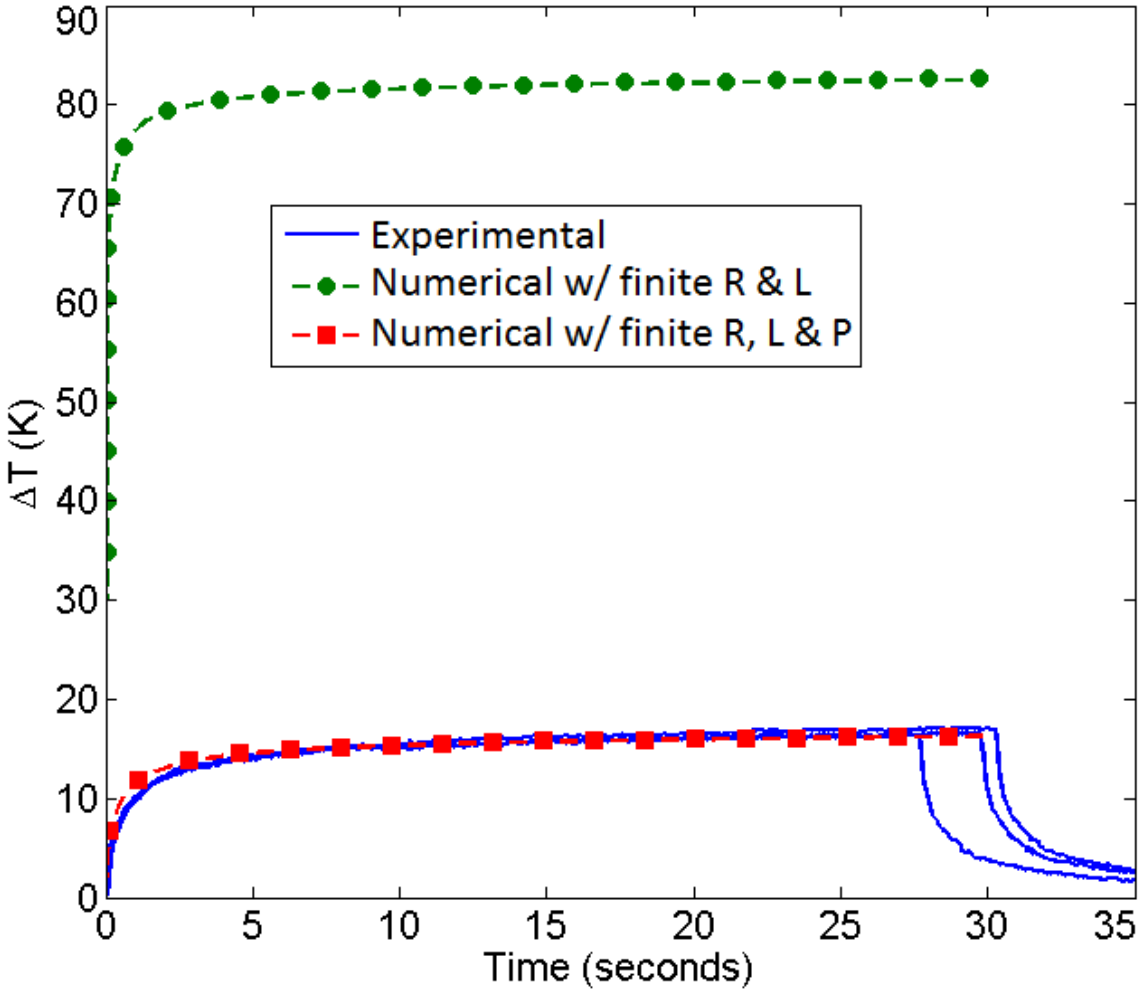

Figure 2.6 Laser heating of SiO_2 1 inch optical flat with HR HfO_2/SiO_2 DBR coating and non-ideal thermal camera properties. P_{laser} = 15.5[kW], absorption = 6[ppm], w = .15[mm], c = 703[J/(kg·K)], ρ = 2648[kg/m^3], k = 1.5[W/(m·K)], α = 8.06x10-7[m^2/s], P_s = 2mm.

From Figure 2.6 we can see that having a pixel resolution much greater than the laser beam width can result in very different readings from what actually occurred. The model also provides a method to extract an accurate reading of absorption regardless of experimental parameters. The final model of equation (2.3.3) with all experimental corrections can fit experiments with all spot sizes without varying absorption as was done in the previous models in Figure 2.2, 2.3 and 2.5.

Chapter 3

Laser Damage of Contaminated Optics

In Chapter 2 dynamic thermal distributions from CW laser impulses were studied for materials with time independent properties. In this Chapter time dependent absorption will be introduced to model a change in the materials absorption over time. Most of the parts of this chapter are taken from a publication under review [31]. For most optical elements in lasers, the intrinsic absorption of the optics will not change over the short duration during a laser pulse. However, in the presence of contaminants and large local absorptions, extremely high local temperatures may be able to produce a number of free

carriers in a small local area, changing the total absorption in the system, and the model introduced in Chapter 2 will no longer hold.

In dirty environments where contamination is prevalent, lasers are typically significantly underpowered in order to optimize operational uptime, severely limiting the power output of the laser, or have extremely expensive optics made from diamond [32,33]. This is due to some contaminants that cause orders of magnitude reductions in the LDT of certain optical materials, leading to extensive cleaning or replacement that further limit the operational time in the field. The new model presented in this Chapter which takes into account time dependent absorption is further modified to predict the effect of certain contaminants on the LDT of the optic. This presents the first physical theory of contamination-induced CW laser damage, rather than treating the problem statistically. With a physical theory of why lasers fail in these environments, the optical system design can then be optimized for more contamination resilient materials.

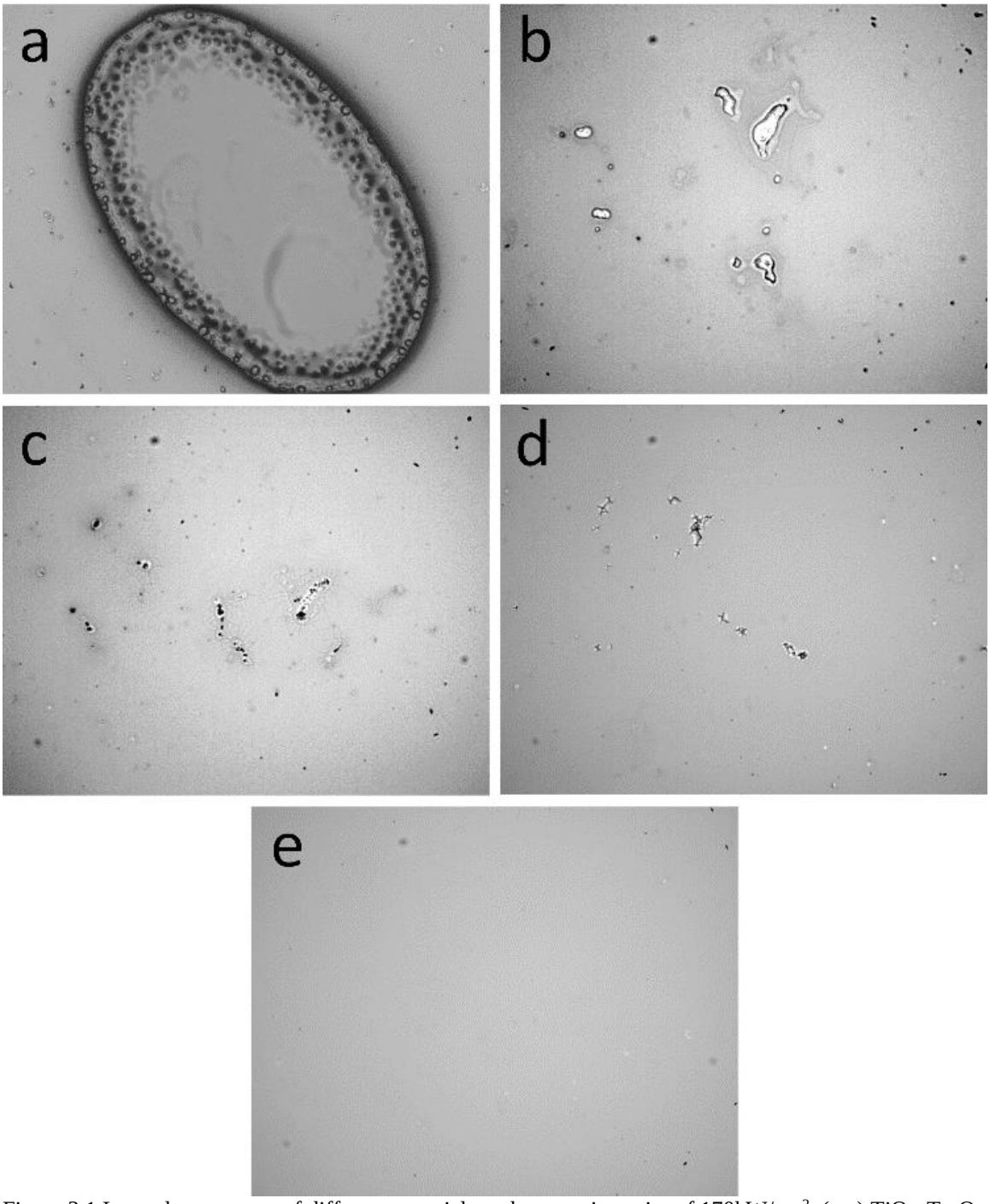

Figure 3.1 Laser damage tests of different materials at the same intensity of 170kW/cm^2. (a-e) TiO_2, Ta_2O_5, HfO_2, Al_2O_3, SiO_2 respectively. The images also correspond to increasing bandgap from a to e.

It is theorized that under the right conditions a particulate, defect, or contaminant will absorb incident high power laser light creating a large local temperature extreme, whereby the thermal energy can conduct into the underlying optic and create thermally excited free carriers. Because of the typically large bandgap in most optical materials used in high power CW lasers, the laser light cannot typically be absorbed by exciting carriers without the extremely large intensities required for multiphoton absorption or bandgap collapse shown in Figure 3.2A and B. However, in a local area where thermally generated free carriers are present, the low energy photons can now be readily absorbed without requiring the statistically unlikely event of multiphoton absorption as seen in Figure 3.2C. It is easy to see then that the thermally generated free carriers cause more absorption, leading to more thermal energy, and produce to more free carriers in a thermal runaway process. This runaway process is then theorized to eventually cause the catastrophic failure in optics under high power CW illumination when contaminated.

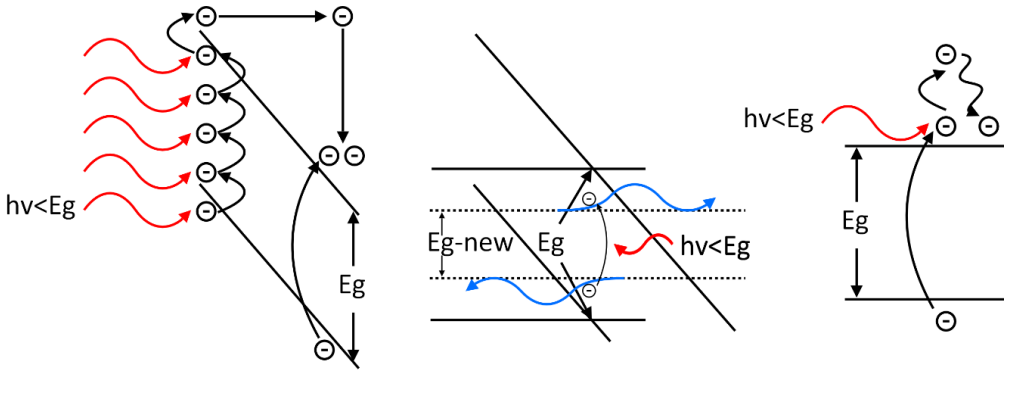

Figure 3.2 Selected absorption processes of low energy photons in high bandgap materials. (A) The multiphoton absorption process and impact ionization in the presence of a large electric field (not present in the CW case). (B) Bandgap collapse due to the Franz-Keldysh effect, where the carrier wave functions leak into the bandgap, again this is only present in large electric fields. (C) Thermally generated free carriers and absorption in small electric fields.

3.1 Laser Damage Tests

In order to test if thermally generated free carriers can in fact be created and cause thermal runaway, a highly absorbing contaminant with a very high melting and evaporation point is needed. A large absorption is required in order the convert the photon energy to thermal energy in the sample. A large melting and evaporation temperature is needed so that the temperature in the optic can be increased to a point where free carriers can be thermally generated before the contaminant itself leaves the surface. Carbon happens to be a common contaminant in most environments on earth, with a large absorption coefficient at 1μm wavelengths, and does not sublimate until extremely high temperatures are reached.

In experiments performed at the EOC, with the same laser described in Section 2.2 optical materials tested were oxides typically used in high power laser systems because of their low intrinsic absorption values (TiO_2, Ta_2O_5, HfO_2, Al_2O_3, and SiO_2). The optics were mounted on an x-y moveable stage to change their position between every 30 second laser shot to prevent the overlap of the current shot with the area of effect of any previous shot. The laser was described previously in Chapter 2. Most tests were done at a spot size of 1mm with an output irradiance range of 20kW/cm^2 to 3MW/cm^2. The contaminated optics were tested starting at 20kW/cm^2 then 50, 80, 110, 140, 170, 200, 300, 400, 1000, 1500, 2000, 2500, and 3000. After each shot the optic was moved: if a damage event occurred, testing stopped, and the optic was moved at least 8mm away from the damage location to move outside the range of any ejected debris.

This was repeated up to 3 times per material, except Ta_2O_5, which was tested significantly more due to the large number of substrates with the material available. The LDT could hypothetically be defined by any one of three methods: average maximum survivable intensity, average minimum failure intensity, 50% failure intensity. In this work, the average minimum failure intensity was used since it is the closest representation of what the model in this Chapter can simulate.

Optics were contaminated with 25-50μm carbon particulates at 10-25 particles/mm^2. The optics were contaminated by pipetting an amalgamation of the particles and acetone onto the surface until it was covered. The optics sat for 1min to let the particulates settle onto the surface uniformly, the left over amalgam was then blown off with an N_2 gun. The amalgam was agitated vigorously before each pipetting to ensure none of the particles had settled in the container before being deposited on the optics. The distribution of particles was examined under an optical microscope to ensure similar distributions across different samples.

Salt was also a candidate for contamination although it has a low absorption coefficient. Salt is a very prevalent contamination however on naval mounted high power laser systems. In these tests salt was deposited either by mounting optics on naval ships for a month or from a simple salt spray in the lab and then allowed to evaporate leaving the salt crystals behind.

In other tests gold nanoparticles were used due to their low variance in manufacturing irregularities. These particles, unlike salt and carbon, actually reflect most

of the light resulting in relatively small amounts of absorption. Gold also has a low melting and evaporation point which is also undesirable for this experiment. For these reason carbon particulates are used most often in experiments.

Contaminated Al_2O_3 and SiO_2 did not catastrophically fail in any test. SiO_2 was tested up to 17.8MW/cm^2 but that required a reduction in spot size to reach that intensity. Later it will be shown that a change in spot size may affect the contamination-induced LDT of the optic. All pristine optics were tested to 3MW/cm^2 with a spot size of 1mm, and all survived.

3.2 Time Dependent Laser Heating

To understand the runaway free carrier generation mechanism proposed, a model of time dependent laser heating will first be needed. A method for time-independent absorption laser heating has been presented and shown to work well for ultra-low absorption optical films with low thermal conductivities in Chapter 2 above [10–12,28]. Equation (3.2.1) has been modified from (2.1.6) for the time-dependent case, and *r* has been set to zero.

$$\Delta T(z,t) = \frac{1}{2\pi^{3/2}\rho c\sqrt{\alpha}} \int_0^t \frac{P(t-t')A(t-t')\exp\left(\frac{-z^2}{4\alpha t'}\right)}{\sqrt{t'}(w^2+2\alpha t')} dt' \qquad (3.2.1)$$

If total power absorbed, *PA*, is time dependent then the product *PA*(*t*) is convolved with the diffusion terms as in equation (3.2.1) rather than just multiplied and integrated as in equation (2.1.6). The convolution in equation (3.2.1) is needed because at *t'=0* (no diffusion yet) the absorption term needs to be equal to the absorption at time *t*, (the end of the CW pulse) *A*(*t*), because that "pulse" at time *t* has not yet diffused, it has

just been absorbed; at time $t'=t$ (diffused for t time) the absorption term needs to be equal to the absorption at time 0, (the beginning of the CW pulse) $A(0)$, because that "pulse" at time 0 has diffused for t amount of time. The same argument holds for time dependent power of the laser, thus the total time dependent power absorbed, $P(t)A(t)$, is convolved with the diffusion terms.

If the catastrophic failure of optics under CW laser illumination is due to thermal shock then Equation (3.2.1) can be used to find thermal gradients. The thermal gradients can then predict when optics would be at the highest risk for thermal shock induced failures. There is no known solution to Equation (3.2.1) in general, but if the surface (z = 0) is examined then solutions can be found. Now the thermal shock is considered as a large difference in temperature between two moments in time, rather than two locations in space.

Consider the onset of lasing, where the ramp is described as a polynomial of order m. The total power absorbed by the optic can then be modeled as $P_{\text{final}}(A)(t^m)$ where small values of m correspond to a fast turn on time, and large values of m also correspond to a fast turn on time but offset and orthogonal to the small values of m. In this treatment only times between 0 and 1 should be considered so that the power-absorbed term is always equal at time t = 1 for any m. This shows the temperature profile for different ramps up to a given power level. After time t = 1 the temperature profile will approach the steady state solution given in Equation (2.1.10). Equation (3.2.1) can now be modeled as the following.

$$\Delta T(t) = \frac{1}{2\pi^{3/2}\rho c\sqrt{\alpha}} \int_0^t \frac{PA\left(t - t'^{m}\right)}{\sqrt{t'}(w^2 + 2\alpha t')} dt' \\ = \frac{PAt^{1/2+m}}{2\pi\rho c\omega^2\sqrt{\alpha}} \frac{\Gamma(1+m)}{\Gamma\left(\frac{3}{2}+m\right)} \, {}_2F_1\left(\frac{1}{2}, 1; \frac{3}{2}+m; \frac{-t\alpha}{\omega^2}\right) \tag{3.2.2}$$

The solution to Equation (3.2.2) is only valid for the power ramp and involves hyper geometric functions and gamma functions but the take away should be what happens as a function of time and *m*. Below in Figure 3.3, Equation (3.2.2) can be visualized for different values of *m*. Notice from Equation (3.2.2) that the parameters with the most effect on the overall shape of the curve in Figure 3.3 are the thermal diffusivity and laser spot size. Larger thermal diffusivities have a similar effect as smaller spot sizes in the resulting curve shape from Equation (3.2.2) where the curves spread out more. However, larger thermal diffusivities cause a decrease in temperature, whereas smaller spot size cause an increase in the temperature.

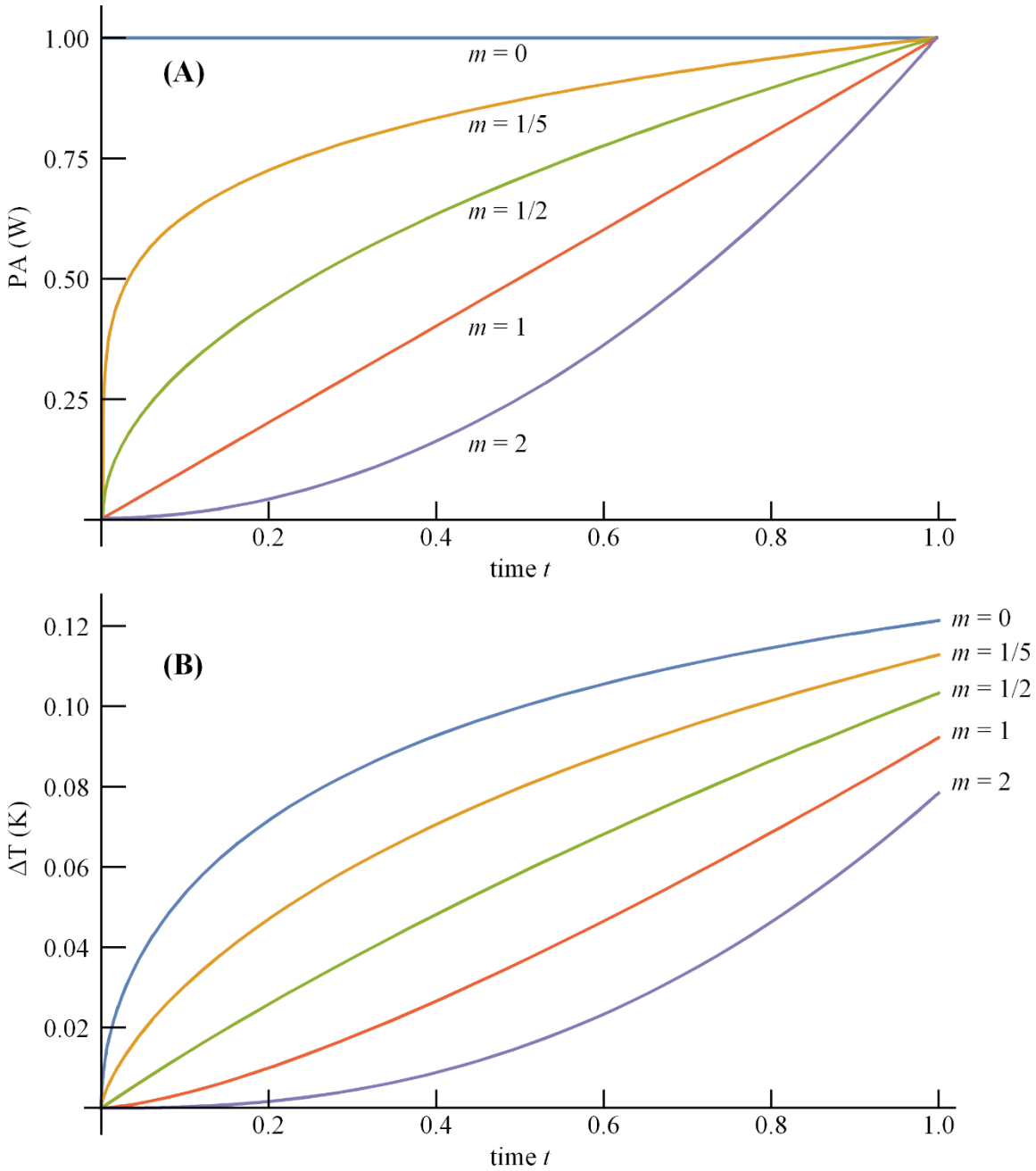

Figure 3.3 Graph of laser surface heating of optics (B) with polynomial power ramps of order m (A). Plot was created using Equation (3.2.2) with $P{\cdot}A = 1$, $\rho = 1$, $c = 1$, $\alpha = 1$, $\omega = 1$.

In order to uncover any features of Equation (3.2.2) that may point to thermal shock, the derivative with respect to time will need to be taken.

$$\frac{d\Delta T}{dt} = \frac{PAt^m}{4\pi\rho c\omega^4\sqrt{t\alpha}} \frac{\Gamma(1+m)}{\Gamma\left(\frac{3}{2}+m\right)\Gamma\left(\frac{5}{2}+m\right)}$$
$$\times\left((1+2m)\omega^2\ {}_2F_1\left(\frac{1}{2},1;\frac{3}{2}+m;\frac{-2t\alpha}{\omega^2}\right)-2t\alpha\ {}_2F_1\left(\frac{3}{2},2;\frac{5}{2}+m;\frac{-t\alpha}{\omega^2}\right)\right) \quad (3.2.3)$$

At this point the limit of Equation (3.2.3) as *t* goes to *0* is desired, unfortunately the limit does not exist. However if *m* is set to a value then the limit can be found. The limit for laser heating ramps with $m < 1/2$ goes to infinity, and for $m > 1/2$ goes to 0, while for $m = 1/2$ the slope goes to a finite number given by the following equation.

$$\lim_{t\to 0}\left(\frac{d\Delta T}{dt}\right)_{m\to 1/2} = \frac{PA}{4\rho c\omega^2\sqrt{\pi\alpha}} \quad (3.2.4)$$

What the limit proves is that a ramped initial power turn on with $m \geq 1/2$ is desired to decrease the chance of problems arising from thermal shocks. The rate of power increase has not yet been incorporated into the model. To incorporate the time rate of change the power term *P* will need to be edited to P/t_{max}^m to reflect a rate, where t_{max} is the time it takes for the ramp to reach full power *P*. carrying the change forward to all equations results in Equation (3.2.4) being changed to the following.

$$\lim_{t\to 0}\left(\frac{d\Delta T}{dt}\right)_{m\to 1/2} = \frac{PA}{4\rho c\omega^2\sqrt{t_{max}\pi\alpha}} \quad (3.2.5)$$

Contaminated Tantala films were tested with a linearly ramped CW laser to see if the LDT could be increased. The results showed that for a ramp of less than 30kW/cm^2/s and a 1mm spot size the LDT increase by an order of magnitude from about 200kW/cm^2

with infinitely fast ramps to >2,500kW/cm^2 with the slower ramps on the order of 50kW/cm^2/s.

Thermal shocks seem to be part of the CW contamination-induced laser damage mechanism but cannot fully describe all damage mechanisms. Using different materials in the laser damage tests with infinitely fast ramps shows no correlation to a materials melting point, boiling point, or thermal shock resilience as defined by the following equation [34,35].

$$R_T = \frac{k\sigma_t(1-\nu)}{\alpha_{ex}E} \tag{3.2.6}$$

In the previous equation R_T is the thermal shock resilience of a material, k is the thermal conductivity, σ_t is the tensile strength, ν is the Poisson ratio, α_{ex} is the thermal expansion coefficient, and E is the Young's Modulus of the material. The rest of the CW laser damage theory needs to incorporate non-linear mechanisms such as free carrier generation and absorption to further understand the damage process.

3.3 Contamination-Induced Free Carrier Absorption model

Thermally generated free carriers have seldom been examined in transparent oxides since the bandgaps are so large that extreme temperatures need to be reached to generate significant densities of carriers. The thermally generated free carrier density, n, is given in equation (3.3.1) and shows that n is exponentially dependent on both temperature, T, and material bandgap, E_G, where k_B is the Boltzmann constant [36].

$$n \propto T^{3/2}\exp(-E_G/2k_BT) \tag{3.3.1}$$

Equation (3.3.1) predicts that when highly absorbing particulates interact with high power CW lasers, extreme localized heating will cause a significant number of free carriers to be generated in a local zone. The localized free carriers can in turn absorb a photon and release the energy via phonon scattering, causing more localized heating and generating more free carriers in a runaway process [37–40]. A subtlety in equation (3.3.1) is that the bandgap is also affected by temperature as shown in equation (3.3.2), reducing slightly as T increases because of the increase in the lattice constant due to thermal expansion [41]. Other factors can reduce the bandgap further such as photoionization and bandgap collapse due to the Franz-Keldysh effect and Mott transitions, but these only occur at much higher fluences and require pulsed lasers to produce such high intensities [42,43]. The bandgap can be defined as a function of temperature as:

$$E_G = E_{G0} - \frac{\alpha_{E_G} T^2}{\left(T + \beta_{E_G}\right)} \tag{3.3.2}$$

where E_{G0} is the band gap at *0* Kelvin, α_{EG} and β_{EG} are constants used to experimentally fit band gap data. (Data on the variation on bandgap with temperature is extremely scarce in the literature, so an ad hoc assumption is used to obtain rough numbers for fused silica and then carried over to every material analyzed. The ad-hoc assumption is that since fused silica has a thermal expansion coefficient that is about a factor of 10 lower than that of Si, the bandgap is modeled with temperature dependence only one tenth that of silicon [41,44].)

The significant unknown variable in the model at this point is the time dependent absorption of the optic, $A(t)$. To handle this, the free carrier absorption coefficient, a, will

be modeled as directly proportional to the free carrier concentration for simplicity as in the following equation (3.3.3), although some references have reported other behavior [45,46]:

$$a(z,t) = K_i \lambda^3 n(z,t) \tag{3.3.3}$$

where K_i is usually experimentally fit to data but is only estimated here, λ is the wavelength of the laser, and n is the number of free carriers. It is important to note that the absorption coefficient is dependent on depth into the material but it is still assumed that all the absorption occurs at the surface. This inconsistency is immaterial since the thermal diffusion depth is very small during thermal runaway. The total time dependent absorption, $A(t)$, can then be calculated from equation (3.3.4) where A_i is the room temperature materials absorption (obtained from optical constant values in the literature), and L is the thickness of the material.

$$A(t) = A_i + 1 - \exp\left(-\int_0^L a(z,t)dz\right) \tag{3.3.4}$$

For simplicity, the optical thickness of the material is considered constant; that is, L is normalized relative to the refractive index. This typically means that higher bandgap materials will be slightly thicker since there is usually an inverse linear relationship between the refractive index and effective bandgap of the oxides [47]. Unfortunately, however, the thermal generation of free carriers and free carrier absorption are dependent on the local temperature of the optic which can only be calculated if the absorption is known. Numerical computation techniques can be used to iteratively solve the problem quickly as seen in Figure 3.4.

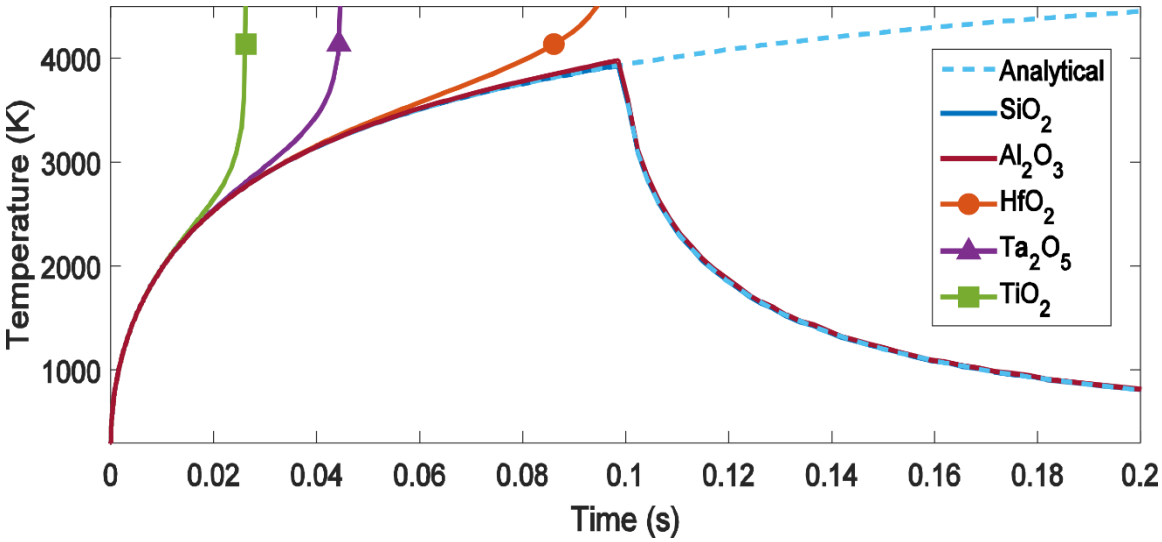

Figure 3.4 Plot of thermal response to CW laser heating for materials with different bandgaps. The analytical curves represent a constant power absorbed term where the laser turns off at t = 0.1s, with an intrinsic absorption of 900ppm. The lower band gap materials follow the analytical solution up until a point where free carrier absorption runs away. The intrinsic absorption goes to 0 at t = 0.1s (representing an evaporating particle) showing the model fits the analytical solutions for time varying absorptions where the high band gap materials follow the analytical result for self-quenching after the laser turns off.

One of the most common environmental contaminants are carbon-based compounds. These are seen in everything from fingerprints to atmospheric aerosols [14,15]. Consider a carbon graphite particle ~25μm in radius as a contaminant. This particle will absorb nearly 100 percent of the incident laser light from a ytterbium-doped fiber laser emitting 1070nm light described in 2.2 above. Graphite has a well-defined vapor pressure, P_e, from which a rate of reduction in radius, Δr, can be calculated from the temperature if the particle is assumed to be a hemisphere lying flat against the optic as in Figure 3.5 [48–50]:

$$\Delta r = \frac{\Delta t P_e}{\rho}\sqrt{\frac{M}{2\pi k_B T}} \tag{3.3.5}$$

where, M, is the molecular mass of the particle in equation (3.3.5). The net thermal power gained, P_{tot}, by the particle can be modeled as $P_{tot} = P_{in} + P_{in}^{rad} - P_{out}^{rad} - P_{out}^{cond} - P_{out}^{conv}$ where P_{in} is the power incident from the laser, P_{rad}, P_{cond}, and P_{conv} are the thermal power loses of radiation, interface conduction, and convection. The temperature of the particle will then be given by the energy gained divided by the heat capacity of the particle. The power lost to interface conduction can be incorporated into equation (3.2.1) and the model will be complete for the ideal case.

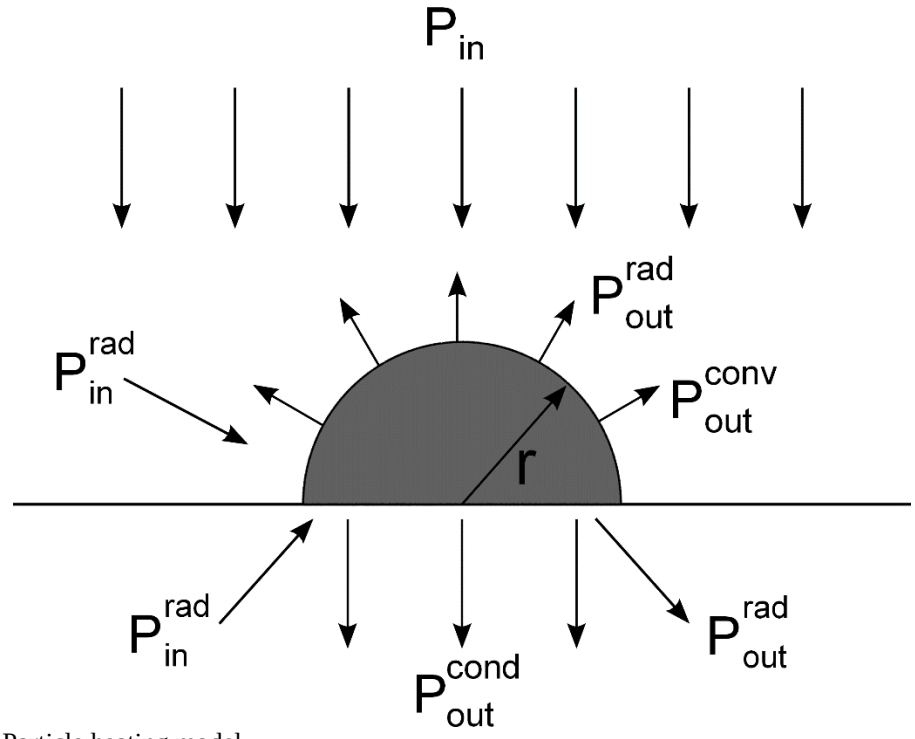

Figure 3.5 Particle heating model.

Photothermal Common path Interferometry (PCI) measurements and microscopy images also show that after the particulate evaporates or sublimates there is a left over residue with a non-zero absorption. The residue can be incorporated into the model by

adding a ring of absorption around the evaporating particle which induces an extra power in addition to P_{cond} into equation (3.2.1).

The issue of thermal contact conductance between contaminant and surface must still be addressed. The interface contact conductance varies from contaminant to contaminant, even if two particles are geometrically alike. Differing thermal contact conductance makes it difficult to use a common simulation value across all materials and modeling situations. Some pulsed PCI measurements even suggest interface contact conductance changes over time for a given particle. Multiple particulates randomly located within the laser spot, affecting each other through thermal diffusion further compounds the experimental difficulties.

Nevertheless, the model can be used to simulate a theoretical situation where all the variables are known and only one particle is within the laser spot. Figure 3.6 shows how a 500μm particle on a Si substrate might react when hit with a 9kW laser with a 1mm beam radius. It is interesting that the substrate will start to generate free carriers and add to the absorption, causing the substrate to heat more readily than the particle around 150ms. This heat then conducts back to the particle making it hotter and causing it to evaporate more quickly. Even after the particle completely evaporates there are enough free carriers present to further heat the Si substrate and cause thermal runaway. The temperatures simulated here are much larger than the melting point of Si. For larger intensities the temperatures can be lower as fewer free carriers are needed to cause the same level of heating.

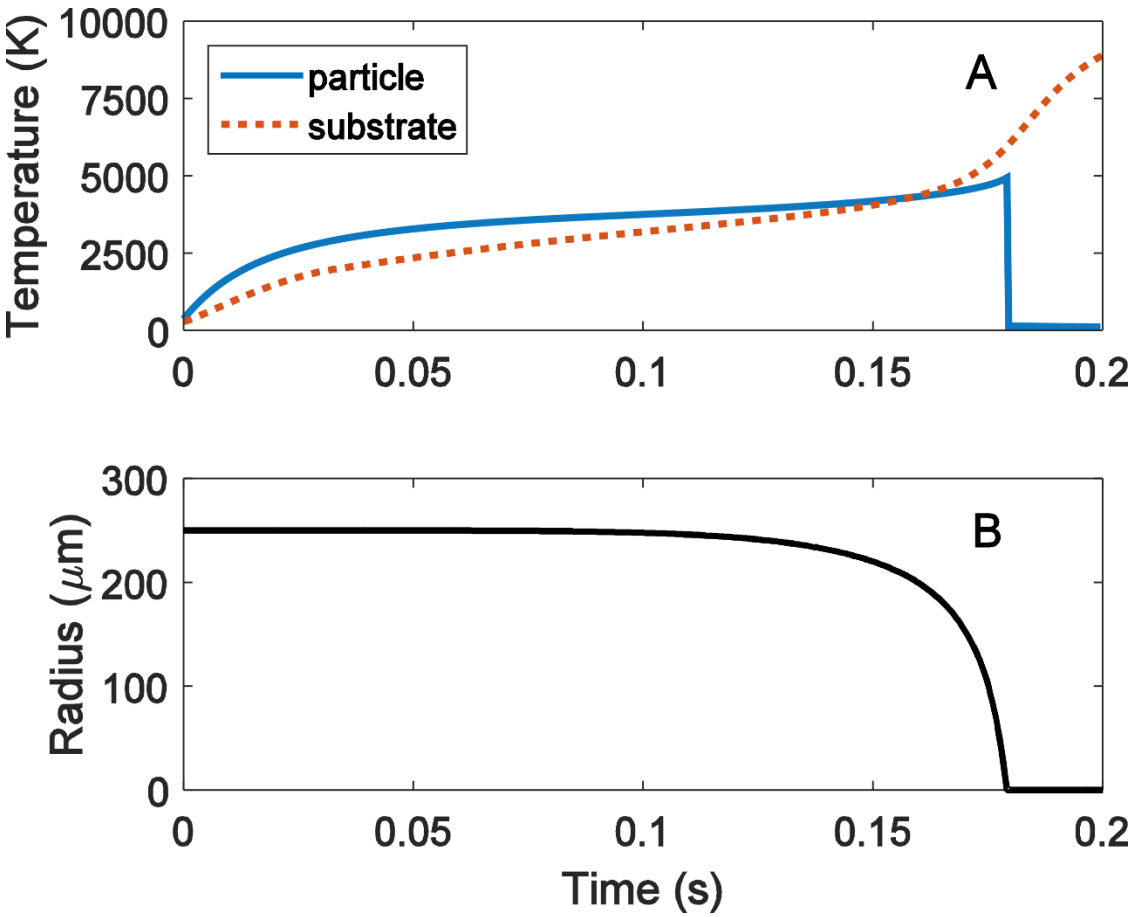

Figure 3.6 Particle heating simulation. (A) The temperature of the particle and substrate directly below the particle are plotted. (B) The radius of the particle as it undergoes laser heating. The simulation parameters were 9kW laser heating a carbon particle on Si with, w = 1mm, h_c = 40,000W/m^2/K, with the particle absorbing 42% of light before sublimating and absorbing 500ppm after.

As a simplification from the current model, a virtual particle will be assumed to heat slowly such that the heat can diffuse through a coating (TiO_2, Ta_2O_5, HfO_2, Al_2O_3, or SiO_2) on a silica substrate. The thermal diffusion time $\tau = L^2/\alpha$ of a half wave, 360nm silica coating is 161ns. Therefore since diffusion is so fast for a thin film, the "slow" heating model is reasonable, directly transferring heat. The virtual particle will heat at a rate of 24,000K/s or about 4mK per 161ns regardless of laser fluence. This simulates how a coating will react to a given temperature and fluence. When a thermal coefficient of the

coating material is not available from the literature, it will be assumed to be similar to that of silica. In all cases, the bandgaps of the materials are known.

As the film heats, equation (3.2.1) will be used to simulate the temperature of the material. At low temperatures, the temperature of the coating simply follows that of the virtual particle as there are few thermally generated free carriers. As the temperature and thus free carrier density increases, direct absorption of laser light by the carriers of the coating becomes possible.

The model, at its simplest, describes whether or not an optic with the thermal properties of fused silica and a given bandgap will thermally runaway under a laser illumination if a certain temperature is reached within the optic. The rate at which the temperature increases is shown in Figure 3.7a for a variety of coating material bandgaps and a laser intensity of 100kW/cm^2. The onset of thermal runaway temperature is defined as the point where the concentration of thermally generated free carriers starts increasing faster than if the temperature simply followed the temperature of the virtual particle. This point is found by minimizing the derivative of the log of free carrier density versus time. The model can then be tested for a range of bandgaps and laser intensities, and a thermal runaway temperature can be derived as a function of bandgap and laser intensity as shown in Figure 3.7b.

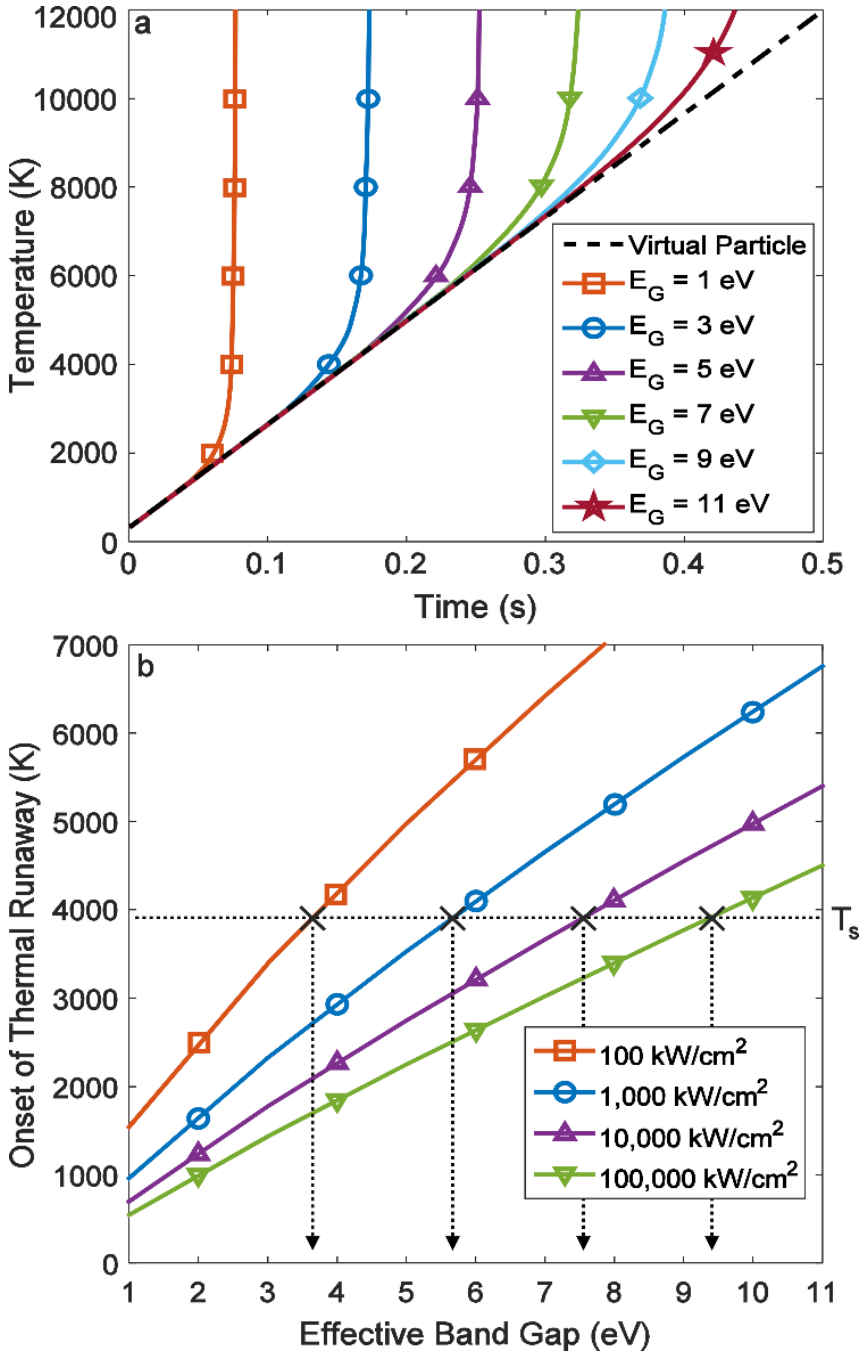

Figure 3.7 Modeling of thermal runaway due to free carrier generation and absorption. (a) Temperature of the center of the laser beam at the surface of the optic. The inflection point where the lines begin to curve up is the onset of thermal runaway. (b) Onset of thermal runaway as a function of bandgap and intensity. The horizontal line, T_s, and intersection points are a prediction of laser damage threshold (LDT) for contaminated optics as a function of bandgap. Note that the value of T_s in this simulation is set by the sublimation point of carbon particles.

Figure 3.7b requires further explanation. This plot assumes that a particle with a certain sublimation or vaporization temperature exists on the surface. In this case, the particle is carbon since it is used in experiments to be described momentarily. Carbon is known to sublimate at 3,900K at 1atm pressure [51]. Since laser heating is a dynamic process, it may be that the internal temperature of the particle far exceeds this because thermal equilibrium certainly cannot be assumed. It has even been shown in some laser damage tests that materials reach 12,000K [52]. For simplicity, however, the sublimation temperature of the particle will be assumed to be the maximum temperature transferred to the substrate immediately below it. Therefore, the carbon particle transfers heat and generates a certain concentration of free carriers. Large bandgap materials will have fewer thermally generated free carriers while small bandgap materials will have more. The intensity of laser light necessary to cause significant heating of the coating material will therefore vary with bandgap. Very high intensities will be necessary to breakdown a high bandgap material while much lower intensities will suffice for small bandgaps. An increase in laser intensity would cause thermal runaway at lower temperatures for a material of the same bandgap and a decrease in intensity would not cause thermal runaway for that level of free carrier generation and absorption. The intersection points can be plotted as LDT as a function of bandgap in Figure 3.8.

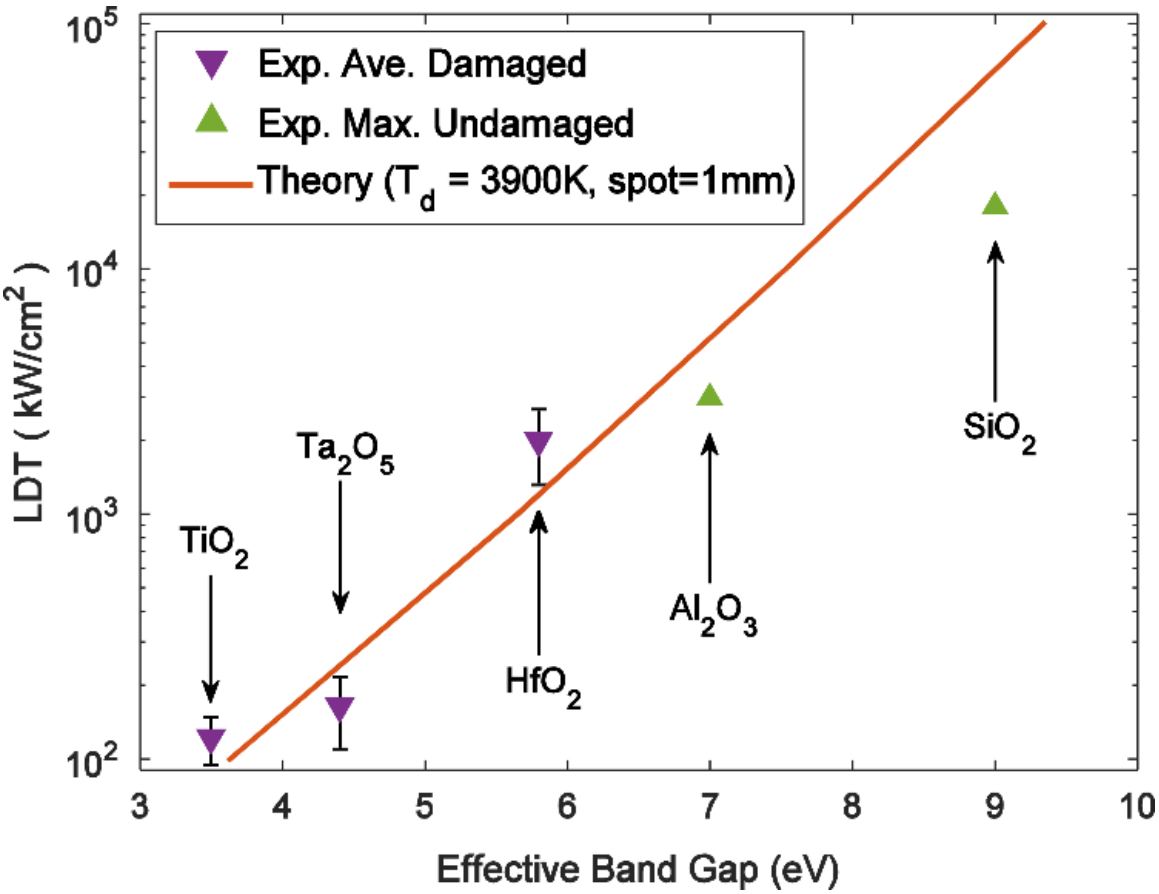

Figure 3.8 LDT for contaminated optics as a function of bandgap. The damaged experimental points are calculated as the average minimum intensity required for catastrophic failure with 1σ vertical error bars. The undamaged experimental points are the maximum intensity tested as none of the samples catastrophically failed, SiO_2 was tested up to 17.8MW/cm^2 but a reduction in spot size was require to achieve that intensity. The line is based on theory for an onset of damage temperature of 3,900K, 1mm laser spot, and fused silica material properties.

Experiments to test this model were performed using roughly size-sorted 99.99% pure carbon as contaminant particles. The particulates varied between approximately 20 and 50 microns in diameter.

Experimentally finding the LDT of different films with contamination in the lab was done with hundreds of laser damage tests. Each optic and film were first tested with no contamination and survived the highest irradiances available, 3MW/cm^2, to show that when a damage event occurs with contamination it would be due to the contamination

and not the film itself. Each optic was then contaminated and tested by starting at a low irradiance and increasing the irradiance of the laser shots. No two shots could overlap spatially as particulate contamination has a strong conditioning response in both pulsed and CW laser operation [14,53,54]. Once the optic fails catastrophically the entire optic becomes more heavily contaminated from the ejected material landing back on the optic, so at that point the LDT data is recorded, and a new sample is prepared for testing. After many tests there is a large range of irradiances where sometimes the optic fails and sometimes survives due to the random nature of the particulate contamination. The LDT is then taken as the average minimum irradiance that an optic and thin film failed. A similar result is attained if the LDT is calculated as the average maximum irradiance that an optic survived, or as the point where 50% of the optics survived.

Two of the materials tested, alumina and silica, did not catastrophically fail for any test, but alumina started to look visibly cloudy at high irradiance while silica remained visibly unchanged. Under magnification, alumina showed cracks and other odd feature formations at high irradiances where silica looked pristine even under magnification as was shown in Figure 3.1. The difference between the two materials at high irradiances may be due to mechanical issues rather than free carrier generation as neither of them reached a high enough temperature to breakdown due to free carrier processes.

3.4 Model Predictions

The primary prediction of the model is the strong dependence of contamination-induced LDT on bandgap, and this prediction is currently borne out in the experimental data of Figure 3.8. The intrinsic absorption of the optical material would seem to play no role in contamination-induced breakdown, so the choice of low absorption materials to reduce in-use heating under CW illumination may actually contribute to early failure as some low absorption materials, such as Ta_2O_5, have relatively small bandgaps.

Interestingly the model also predicts a strong correlation between the temperature that a given contaminant produces, T_s, and the LDT of the optic. If a contaminant produces a lower T_s than carbon, the model predicts larger LDT's, and a stronger dependence (steeper slope in Figure 3.8) on the bandgap. For higher temperature defects the LDT is decreased and there is a smaller dependence (shallower slope in Figure 3.8) on bandgap predicted by the model.

Another prediction of the model is the effect of spot size on LDT. Varying the spot size of the laser can quite drastically change the dynamic thermal profile of the optic. Higher thermal gradients are created by smaller spot sizes, allowing thermal diffusion to proceed more quickly [55]. The model predicts drastic increases in LDT for spot sizes below a certain transition region. The transition regime corresponds to the thermal diffusion length where τ is the time it takes for the optic to fail after the onset of thermal run away. This occurs between 0.1 and 1.0mm for fused silica substrates as shown in Figure 3.9a. For spot sizes larger than L_d, the LDT only slightly decreases meaning the

total power that the optic can withstand rises with spot size area, which agrees with intuition. For spot sizes below L_d, increasing the spot size does not confer similar increases in the total power the optic can withstand. Experimentally there was only one optic tested for spot size changes where a 1mm spot survived at a peak irradiance of 110kW/cm^2 but a 5mm spot failed at 100kW/cm^2.

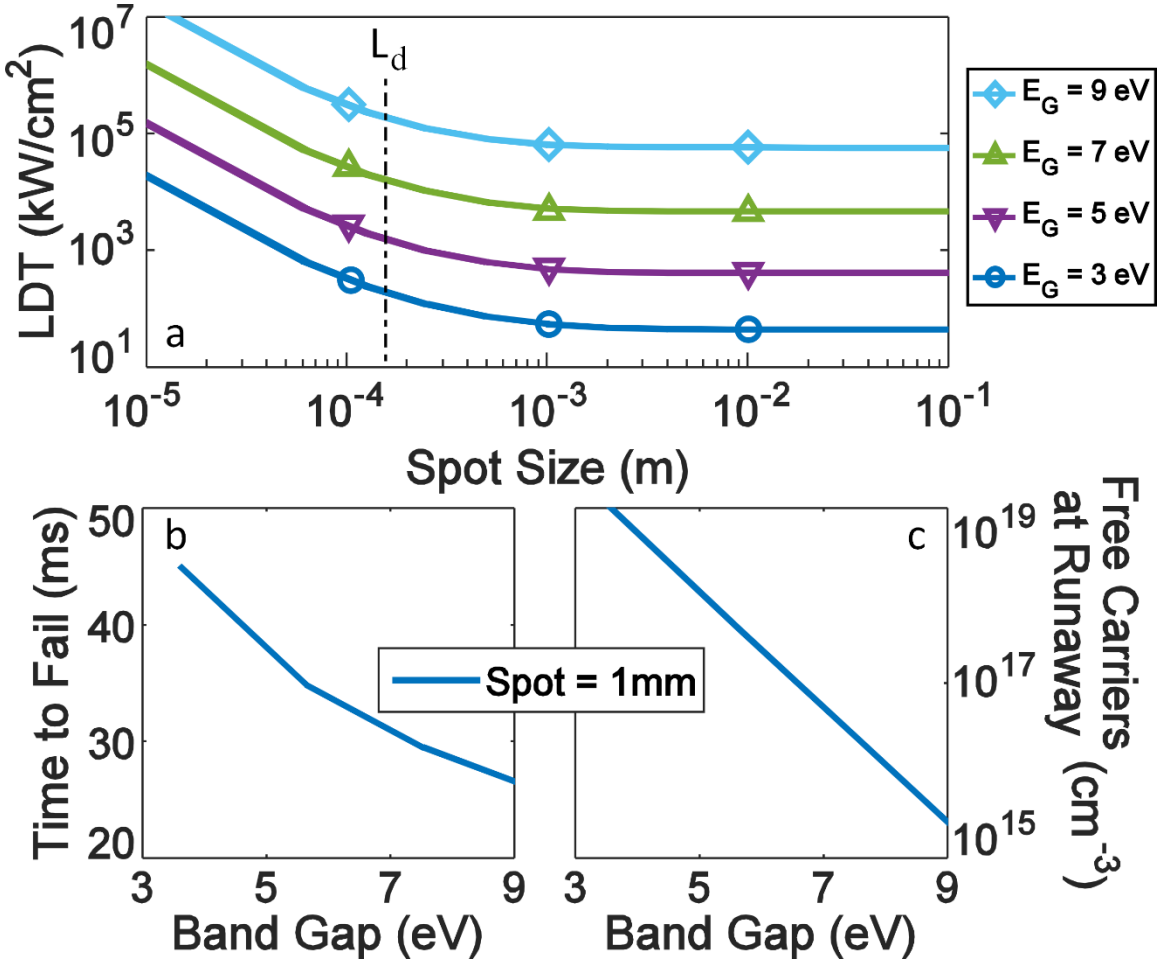

Figure 3.9 Particulate induced laser damage threshold model predictions. (a) Reduction in LDT as an increase in spot sizes below L_d is shown. Spot sizes above L_d show little change in LDT and thus an increase in overall power threshold. (b) Time from onset of thermal runaway to asymptotic temperature behavior. As bandgap increases time to failure decreases because of the higher intensity required to cause thermal runaway. (c) Thermally generated free carriers at onset of thermal runaway as a function of band gap.

Figure 3.9b shows the time scale of thermal runaway due to free carrier generation and absorption. The time to fail is calculated as the time it takes to reach temperatures so high that they are inconsistent with solid-state or molecular substances. For our purposes, 12,000K is chosen somewhat arbitrarily. At higher bandgaps the intensity required to cause thermal runaway increases, causing the runaway time to slightly decrease with increasing bandgap. The thermal runaway time averaged over all bandgaps is on the order of 33ms. The damage mechanism of free carrier generation and absorption predicted by this model would be the slowest process for laser damage compared to carrier excitation, thermalization, thermal and structural events [56]. However, in transitioning to these extreme temperatures, the bandgap may also behave in unexpected ways, Auger recombination may start becoming more dominant, and more defects could be produced increasing the absorption further. All of these could alter the speed of the breakdown process [57].

Figure 3.9c shows the prediction of an exponential decrease in free carrier density at the onset of thermal runaway as a function of band gap. Because the LDT is predicted to increase with the bandgap, and the photon-free carrier absorption events are expected to remain relatively constant at runaway, then the free carrier concentration required for thermal runaway is expected to decrease with bandgap. The free carrier density is predicted to be low enough at the onset of thermal runaway that other non-linear processes such as Auger recombination would not dominate the onset of failure mechanism especially for bandgaps greater than 5eV [37,58].

Chapter 4

Thermal Photon Noise

Thermal photons are produced when the electromagnetic field is coupled to a thermal source of atoms in equilibrium, and the electrons in those atoms change states in order to emit photons. The thermal photons emitted in this process obey Planck's law on average and in this chapter it will be shown why that is as well as how those processes produce noise and the characteristics of that noise. Much of this chapter was taken from a publication under review [59].

4.1 Background

Most particle statistics can be described by one of three ways: Maxwell-Boltzmann (M-B), Bose-Einstein (B-E), and Fermi-Dirac (F-D) statistics. The differences in the

properties of each of these particle statistics come from whether the particles are distinct and distinguishable from one another, and whether or not the particles can occupy the same quantum states. In the case of the photon, the particles are indistinguishable from one another, any number of photons can exist within the same state, and the total number of photons does not need to be conserved in a given system. As an example if there were 2 photons in a system with 3 quantum states there would be 6 ways that the photons could be distributed amongst the states as given by Table 4.1. Also for any number of photons, *n*, and any number of modes, *M*, the number of possible distributions is given by the following equation [60].

$$D = \frac{(n + M - 1)!}{n!\,(M - 1)!} \tag{4.1.1}$$

Table 4.1 All possible ways to put 2 photons in 3 states.

***state* 1**	***state* 2**	***state* 3**
2	-	-
-	**2**	-
-	-	**2**
1	**1**	-
-	**1**	**1**
1	-	**1**

The type of statistics representative of photons and Table 4.1 are Bose-Einstein statistics. However, because photons are not conserved the chemical potential is eliminated from the general B-E statistics. The difference between B-E and the classical Maxwell-Boltzmann statistics is that the particles are distinguishable in M-B statistics,

meaning it is possible to discern when particle 1 and 2 swap states resulting in an additional 3 ways to put 2 particles in 3 states. This means B-E is slightly more restrictive than classical M-B particle statistics. In Fermi-Dirac statistics the particles are indistinguishable like B-E, but the particles are also limited to only 1 particle per state. This results in F-D statistics being the most restrictive distribution.

In the case of thermal photons (ones in which the electromagnetic field is in thermal equilibrium and coupled to a thermal reservoir at a certain temperature T) the photons will also have a probability of existing in the different states represented by the canonical ensemble. Combining the statistics of B-E and thermal photons will allow for a cogent theory of thermal photon statistics.

Assuming that the thermal photons follow the canonical ensemble and obey the Boltzmann distribution where finding a photon in a state or mode above the thermal energy $k_B T$ is less likely, then the probability of finding n_m photons in a mode can be represented by equation (4.1.2) [61].

$$p(n_m) = e^{-n_m h\nu/k_B T}\left(1 - e^{-h\nu/k_B T}\right) \tag{4.1.2}$$

In equation (4.1.2) and the rest of this chapter the following variables are defined as:

- m Mode index
- n A discrete random variable describing the total number of photons in the system
- $\langle n \rangle$ The average total number of photons

- n_m A discrete random variable representing the number of photons present in mode *m*
- $\langle n_m \rangle$ Average number of photons in mode *m*
- h Planck's constant
- v Frequency of light
- c Speed of light in a vacuum
- k_B Boltzmann constant
- T Temperature
- M Total number of modes
- D Total number of possible distributions of *n* photons in *M* modes
- d distribution index

Now that the probability density function is known it is possible to find the average number of photons in a mode using standard statistical analysis as in the following equation.

$$\langle n_m \rangle = \sum_{n_m=0}^{\infty} n_m p(n_m) = \frac{1}{e^{hv/k_B T} - 1} \tag{4.1.3}$$

From equation (4.1.3) it is possible to derive Planck's law of thermal emission by multiplying by the photon energy, hv, and the mode density, $8\pi v^2 \partial v / c^3$, which describes the spectral dependence of thermal light very accurately. Also it would be convenient if equation (4.1.2) was given in terms of the average photon number as is calculated in (4.1.3). After some algebraic manipulation of equation (4.1.3) the following equations are derived [61].

$$e^{-\frac{n_m h\nu}{k_B T}} = \frac{1}{\left(1+\frac{1}{\langle n_m \rangle}\right)^{n_m}}$$
$$1 - e^{-\frac{h\nu}{k_B T}} = \frac{1}{(1+\langle n_m \rangle)} \tag{4.1.4}$$

Substituting the equalities from (4.1.4) into equation (4.1.2) results in the useful representation of the probability of finding n_m photons in a mode.

$$p(n_m) = \frac{1}{(1+\langle n_m \rangle)\left(1+\frac{1}{\langle n_m \rangle}\right)^{n_m}} \tag{4.1.5}$$

Although equation (4.1.5) is mathematically nice and easy to work with it has a few limitations when working with thermal photon noise. The first limitation is that this is valid for a single mode. To incorporate systems with multiple or infinite modes (as is the case in most thermal light applications) the joint probability must be used as in equation (4.1.6). To find the joint probability the probability of finding n_m photons in each mode must be multiplied. However, there is an added difficulty in that there are multiple distributions possible, thus requiring a sum over all the distributions wherein each modal probability is multiplied [61].

$$P(n) = \sum_{d=1}^{D} \prod_{m=1}^{M} \frac{1}{(1+\langle n_m \rangle)\left(1+\frac{1}{\langle n_m \rangle}\right)^{n_{m,d}}} \tag{4.1.6}$$

Here n_m is now $n_{m,d}$ to signify that the number of photons is dependent not only on mode index but also what distribution the photons are in. Already equation (4.1.6) looks much more daunting than (4.1.5), but luckily a simplification exists when a uniform

average photon number, $\langle n_m \rangle$, is used. The product term can be simplified in a few steps, given a uniform average photon number across all modes. First noting that the average total number of photons, $\langle n \rangle$, has to be equal to the sum over all modes of the average photon number in each mode.

$$\langle n \rangle = \sum_{m=1}^{M} \langle n_m \rangle = M \langle n_m \rangle \tag{4.1.7}$$

Plugging (4.1.7) into (4.1.6) gives the following.

$$P(n) = \sum_{d=1}^{D} \prod_{m=1}^{M} \frac{1}{\left(1 + \frac{\langle n \rangle}{M}\right)\left(1 + \frac{M}{\langle n \rangle}\right)^{n_{m,d}}} \tag{4.1.8}$$

The product term can now be rewritten to simplify the equation.

$$P(n) = \sum_{d=1}^{D} \frac{1}{\left(1 + \frac{\langle n \rangle}{M}\right)^{M}\left(1 + \frac{M}{\langle n \rangle}\right)^{\sum_{m=1}^{M} n_{m,d}}} \tag{4.1.9}$$

Independent of distribution the sum over all modes of photons has to be equal to the total number of photons by definition.

$$n = \sum_{m=1}^{M} n_{m,d} \tag{4.1.10}$$

Since the sum, over all modes, of the number of photons in each mode, is equal to the total number of photons as in the above equation (4.1.10), then the product function in equation (4.1.6) will be equal for all distributions, *d*. Substituting (4.1.10) into (4.1.9) allows the product to be calculated once and multiplied by the number of distributions *D*

for the final result of the probability of finding *n* photons in a system given a uniform modal spectrum and is given by the following equation [60,61].

$$P(n) = D\frac{1}{\left(1+\frac{\langle n\rangle}{M}\right)^{M}\left(1+\frac{M}{\langle n\rangle}\right)^{n}} = \frac{(n+M-1)!}{n!\,(M-1)!}\frac{1}{\left(1+\frac{\langle n\rangle}{M}\right)^{M}\left(1+\frac{M}{\langle n\rangle}\right)^{n}} \tag{4.1.11}$$

The variance of the number of thermal photons can now be found using the standard technique defined in the equation below.

$$\langle(\Delta n)^2\rangle = \sum_{n=0}^{\infty}(n-\langle n\rangle)^2 P(n) \tag{4.1.12}$$

Substituting (4.1.11) into (4.1.12) results in the following simple equation for the thermal photon noise.

$$\langle(\Delta n)^2\rangle = \langle n\rangle + \frac{\langle n\rangle^2}{M} \tag{4.1.13}$$

Substituting (4.1.5) into (4.1.12) results in a similar equation but is only valid for single mode systems.

$$\langle(\Delta n)^2\rangle = \langle n\rangle + \langle n\rangle^2 \tag{4.1.14}$$

When the number of modes goes to infinity the thermal photon noise is Poissonian in nature.

$$\langle(\Delta n)^2\rangle|_{M\to\infty} = \langle n\rangle \tag{4.1.15}$$

These results point to thermal photon noise being Poissonian when the average photon number much less than one, and Bose-Einsteinian when the average photon number is much greater than one and the number of coupled modes is small. Situations where non-Poissonian statistics can be found are in microcavities to reduce the number of

modes, and high temperature or low frequency light operation to get large photon numbers as can be seen in equation (4.1.3).

In these situations sometimes single mode operation cannot be guaranteed and the previous derivations have significant setbacks. The main limitation of the previous derivation is that the mode distribution be uniform, meaning all modes have the same expected photon number, $\langle n_m \rangle$. To solve for statistics for cases of non-uniform spectral distribution, a less restrictive simplification is needed, as well as an algorithm for solving for the variance.

4.2 Spectrally Dependent Mode Distributions

The algorithm to be developed here must work for any spectral distribution as seen in Figure 4.1A, as well as any arbitrarily large or small average photon numbers. First it will be useful to examine a simplified square spectral distribution with a single mode with a higher or lower photon population than other modes as shown in Figure 4.1B.

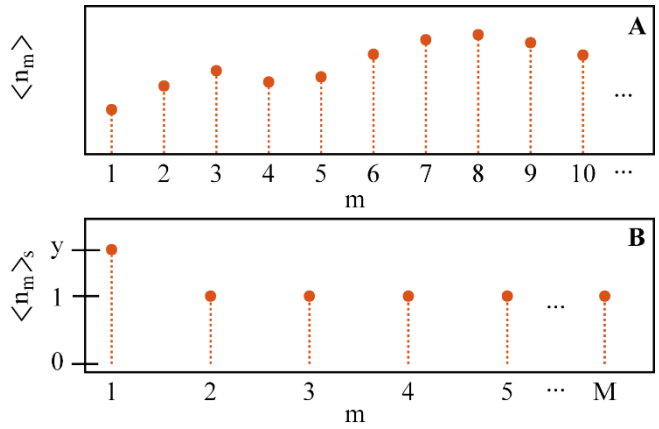

Figure 4.1 Spectrally dependent mode distributions. (A) General modal distribution. (B) Simplified and scaled square distribution. The first mode, m=1, has an average photon number of y, where $y \geq 0$, and all other modes have $\langle n_m \rangle_s = 1$. Note that the photon number in mode 1 can also be less than 1 without changing the quantitative expressions below.

To reproduce the values of the scaled distribution $\langle n_m \rangle_s$ in Figure 4.1B the following equation can be used.

$$\langle n_m \rangle_s = 1 - (1 - y)\delta_{1,m} \tag{4.2.1}$$

In the previous equation $\delta_{1,m}$ is the Kronecker delta function, and y is the fractional height (average photon number) of the first mode relative to the side modes. This situation could represent spectral hole burning in the case of y being small, or a single mode cavity with M-1 side modes and a thermal source when y is large.

Simplification 1. Scale the modal distribution, $\langle n_m \rangle_s$. The mode distribution should be scaled such that the sum over all modes is equal to the expected number of photons, $\langle n \rangle$, as in the following equations:

$$\langle n \rangle = \sum_{m=1}^{M} \langle n_m \rangle = \sum_{m=1}^{M} A \langle n_m \rangle_s \tag{4.2.2}$$

$$A = \frac{\langle n \rangle}{M - 1 + y} \tag{4.2.3}$$

$$\langle n_m \rangle = \frac{\langle n \rangle \left(1 - (1 - y)\delta_{1,m}\right)}{M - 1 + y} \tag{4.2.4}$$

Substituting equation (4.2.4) into (4.1.6) gives a result that already has no known solution, and another simplification is needed.

Step 2. Solve for the probability of having 0 or 1 photons where solutions exist for equation (4.1.6). When n = 0 the photon distribution, $n_{m,d}$, reduces to 0 and equation (4.1.6) simplifies greatly to equation (4.2.5). When n = 1 the photon distribution

simplifies to a Kronecker delta function, $n_{m,d} = \delta_{m,d}$, D simplifies to M, and equation (4.1.6) simplifies to equation (4.2.6).

$$P(0) = \prod_{m=1}^{M} \frac{1}{1 + \langle n_m \rangle} \tag{4.2.5}$$

$$P(1) = \sum_{d=1}^{M} \prod_{m=1}^{M} \frac{1}{(1 + \langle n_m \rangle)\left(1 + \frac{1}{\langle n_m \rangle}\right)^{\delta_{m,d}}} \tag{4.2.6}$$

To find the probabilities of all further numbers of photons is quite difficult. In some situations however, the average number of photons will be small such that the probability will be mostly defined for $n \leq 2$. In that case $P(2) \cong 1 - P(1) - P(0)$ and $P(n > 2) \cong 0$. For the case where $\langle n \rangle$ is exactly zero the probabilities will be exactly correct because $P(0) = 1$ and $P(n > 0) = 0$. As $\langle n \rangle$ becomes larger $P(0)$ and $P(1)$ will always be exact but error is introduced in $P(2)$ because $P(n > 2) \neq 0$. If 99.9999% of the probability is to be contained within $P(n = 0 \text{ OR } n = 1)$ then the average photon number must be less than 1/999 for the case of the spectrum defined in Figure 4.1B. Later an algorithm will be presented for solving for statistics of large expected photon numbers using only the exact probabilities of zero and one photon. It should be noted that the algorithm set forth below does not work if only the $P(0)$ term is calculated exactly and $P(1)$ is estimated to be 1-$P(0)$.

Step 3. Solve for the variance. At this point everything needed (the probability of having 0, 1, or 2 photons) to solve for the variance is available, remembering the result

will only be valid for small expected photon numbers, and is defined by the following equation.

$$\langle(\Delta n)^2\rangle = \sum_{n=0}^{2}(n-\langle n\rangle)^2 P(n) \tag{4.2.7}$$

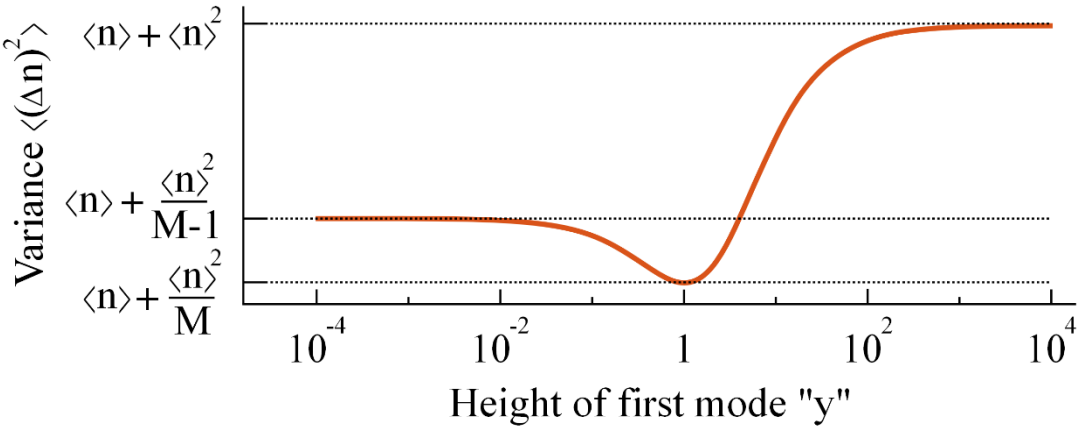

Figure 4.2 Spectrally dependent variance as a function of the height of the first mode. The curve was calculated with M=3, and $\langle n\rangle$=1/999. Curves with other values for M will look similar but the relative heights between the 3 points of y = (0, 1, ∞) will change.

For small expected photon numbers (e.g. $\langle n\rangle < 1/999$) Figure 4.2 will be produced. Figure 4.2 can be intuitively explained from equation (4.1.13) as $y \to 0$ and the number of modes goes to M-1, the variance should be equal to $\langle n\rangle + \langle n\rangle^2/(M-1)$. When $y = 1$ and the number of modes goes to M, the variance should be equal to $\langle n\rangle + \langle n\rangle^2/M$. Finally when $y \to \infty$ and the number of modes essentially goes to 1 as all the side modes are infinitely smaller than the first mode the variance should be $\langle n\rangle + \langle n\rangle^2$. The actual dependence on y everywhere else is not intuitively known but is shown in Figure 4.2.

At this point the actual equation for the variance is quite long and is only accurate for small expected photon numbers and exactly correct for zero expected photons as seen

in the below equation. In the spectral hole burning case a result is needed when the expected photon number is large.

$$\begin{aligned}\langle(\Delta n)^2\rangle &\cong (\langle n\rangle + 2)^2 + Z\frac{(A\langle n\rangle^3 + B\langle n\rangle^2 + C\langle n\rangle + D)}{(M-1+y+\langle n\rangle y)^2}\\ A &= 2(M+2)y\\ B &= (2M^2 - 8y + 5My + 6y^2 - 2)\\ C &= (M-3y-5)(M-1+y)\\ D &= -4(M-1+y)^2\\ Z &= \left(\frac{M-1+y}{M-1+y+\langle n\rangle}\right)^M\end{aligned} \tag{4.2.8}$$

For large photon numbers the curve in Figure 4.2 is expected to be very similar although it has not yet been proven. Solving for the variance of average photon numbers of $\langle n\rangle = 10$ by solving the probability density function (4.1.6) out to $n = 200$, in systems with 2 or 3 modes, reproduces the curve in Figure 4.2 to within 0.01% of the system with $\langle n\rangle = 1/999$ where the probability was only calculated exactly out to $n = 1$. Therefore it is assumed that an analytical expression should produce Figure 4.2 independent of average photon number. Calculating for 100 average photons with 2 or 3 modes would probably be possible using this method in a finite amount of time but for much more photons would take essentially infinite amount of time, therefore an analytical result is needed for more than 100 average photon numbers or more than 3 modes.

To find the analytical expression for the variance for large photon numbers an exact expression is first needed for the case when the limit is taken as $\langle n\rangle \to 0$ other than the trivial answer $\langle(\Delta n)^2\rangle = 0$. What is meant here is that the variance is expected to be a

polynomial in average photon number and the equation and coefficients to that polynomial are desired. To accomplish this goal the curve in Figure 4.2 is first normalized to be invariant with respect to average photon number. That way when the limit of the normalized variance is taken as the average photon number approaches zero, the exact analytical expression for the variance will result.

Step 4. Normalize the variance. Normalizing the variance from equation (4.2.7) and Figure 4.2 to fit between the limits of 0 and 1 can be accomplished by subtracting the minimum value everywhere and scaling by the inverse of the resulting maximum as in the following equation.

$$\overline{\langle(\Delta n)^2\rangle} = \frac{M_1(\langle n\rangle^2 + \langle n\rangle M_0 - M_0\langle(\Delta n)^2\rangle)}{\langle n\rangle^2(M_1 - M_0)} \tag{4.2.9}$$

In the previous equation M_1 is the number of modes when the variance is normalized to 1 (i.e. the maximum of Figure 4.2, where $y \to \infty$, in this case $M_1 = 1$), M_0 is the number of modes when the variance is normalized to 0 (i.e. the minimum of Figure 4.2, where $y = 1$, in this case $M_2 = M$), and $\overline{\langle(\Delta n)^2\rangle}$ is the normalized variance. The analytical result of equation (4.2.9) will still depend on the photon number, although we know from numerical models that the normalized variance should be invariant with respect to average photon number. This is because the algorithm developed thus far is only exactly correct for zero average photons.

Step 5. Find the limit of the normalized variance as the average photon number goes to zero. The analytical limit result is finally independent of photon number and is given by the following.

$$\lim_{\langle n\rangle\to 0}\overline{\langle(\Delta n)^2\rangle} = \frac{(y-1)^2}{(M-1+y)^2} \tag{4.2.10}$$

Step 6. De-Normalize the result. From equation (4.2.10) it is now possible to de-normalize the result and find the final analytical equation for the variance that accurately describes the noise for any photon number, mode number, and first mode height. The de-normalization is given by the following formula.

$$\langle(\Delta n)^2\rangle = \langle n\rangle + \frac{\langle n\rangle^2\left(M_1 + \left(\lim_{\langle n\rangle\to 0}\overline{\langle(\Delta n)^2\rangle}\right)(M_0 - M_1)\right)}{M_1 M_0} \tag{4.2.11}$$

Substituting equation (4.2.10) into (4.2.11) and using the same M_1 and M_0 values as used in the normalization process, gives the final result as seen in the following equation, for the particular spectrally dependent case depicted in Figure 4.1B.

$$\langle(\Delta n)^2\rangle = \langle n\rangle + \langle n\rangle^2\frac{(M-1+y^2)}{(M-1+y)^2} \tag{4.2.12}$$

In the limit of $y = 1$ equation (4.2.12) simplifies to (4.1.13) as would be expected because the spectrum is uniform in that case. In the limit of $M \to \infty$ equation (4.2.12) simplifies to Poissonian statistics where $\langle(\Delta n)^2\rangle = \langle n\rangle$. If in Figure 4.1B the side modes had a photon number equal to z rather than unity then the variance would be given by the following equation.

$$\langle(\Delta n)^2\rangle = \langle n\rangle + \langle n\rangle^2\frac{(z^2(M-1)+y^2)}{(z(M-1)+y)^2} \tag{4.2.13}$$

For the case of a single mode cavity example, where the height of the first mode is 10^3 and there are 9 side modes of height 1, the variance will be $\langle(\Delta n)^2\rangle \cong \langle n\rangle +$

$0.98\langle n\rangle^2$. This shows that equation (4.1.13) would have about a 2% error in the size of the $\langle n\rangle^2$ factor if it was mindlessly applied, when there are 9 side modes 0.1% of the value of the dominant mode.

In the case of spectral hole burning, where the height of the first mode is 0.25 and there are 25 total modes, the variance will be $\langle(\Delta n)^2\rangle \cong \langle n\rangle + 0.0409\langle n\rangle^2$. Again this results in ~2% error in estimates from incorrectly using equation (4.1.13).

If the error between the $\langle n\rangle^2$ factors in equations (4.2.12) and (4.1.13) is taken to be the difference divided by the factor in (4.2.12) then the error for different scenarios can be seen in Figure 4.3. In the worst case where *y* and *M* is very small the error could be as high as 50% for the $\langle n\rangle^2$ factor. Realistically an estimate from (4.1.13) is difficult when *y* is about a half or a couple times bigger than the side modes and errors of 5% to 35% are expected.

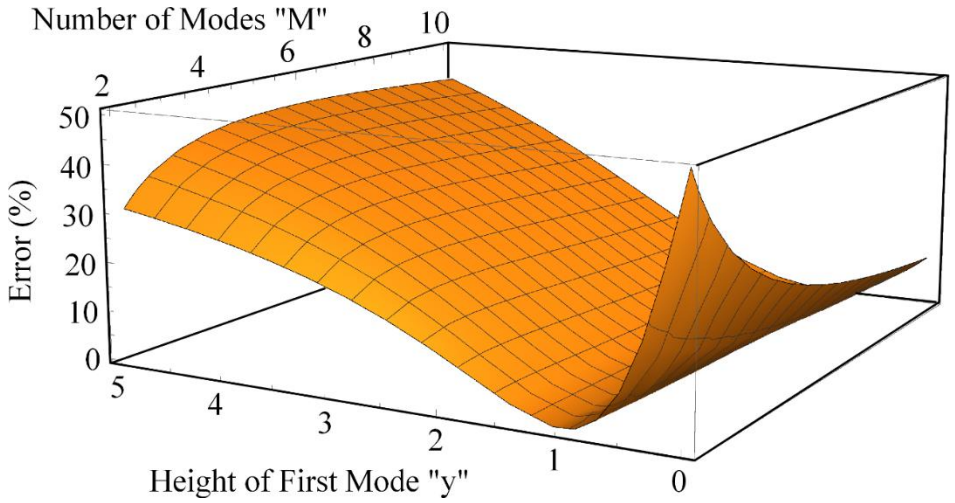

Figure 4.3 The error between the $\langle n\rangle^2$ factors in (4.2.12) and (4.1.13). For large values of *y* an estimation is difficult using (4.1.13) until *y* is so large that a single mode is a good approximation. The error is exactly zero when *y* = 1 because (4.2.12) reduces to (4.1.13).

One interesting takeaway from equation (4.2.12) is what it predicts happens in the situation where there is a single mode infinitely large with infinitely many infinitely small side modes. It is conceivable that a small enough cavity, where only a single optical mode is coupled to a thermal source, would display these properties. The variance will then be given as the limit of equation (4.2.12) as *y* and *M* go to infinity at the same rate. The result is given by equation (4.2.14) and is found by setting $y = M$ and taking the limit as $M \to \infty$. The result is not strictly Poissonian as would be expected with infinite modes, and is not strictly Bose-Einsteinian as would be expected for a single mode cavity.

$$\langle (\Delta n)^2 \rangle = \langle n \rangle + \frac{\langle n \rangle^2}{4} \tag{4.2.14}$$

In general the average photon number in the first mode should not be required to be an integer as in the previous derivation. To allow any average photon number in the first mode *y* can be set to a fraction of *M* by multiplying by a constant *A*. In this case *A* represents the fraction of photons in the first mode relative the total number of photons in all other side modes.

$$\langle (\Delta n)^2 \rangle = \langle n \rangle + \langle n \rangle^2 \frac{A^2}{(1+A)^2} \tag{4.2.15}$$

Finally it should be noted that this algorithm was developed from a first order approximation of the probability density function (i.e. only the probabilities of having 0 or 1 photon in the system is known exactly) resulting in an exact analytical equation. It would be logical to ask if a second order approximation would result in a different more accurate result, and if in fact the analytical results are not exactly correct.

4.3 Second Order and Greater Probability Approximations

Unfortunately finding an analytical representation for 2 or more photons in the probability density function given in equation (4.1.8) is not straightforward. However, if the number of cases is limited to only 2 modes the photon distributions can be found analytically as shown in Table 4.2 and equation (4.3.2). With the number of modes restricted to 2, the number of possible distributions is also simplified to the following equation.

$$D = n + 1 \tag{4.3.1}$$

In the following Table 4.2 the distributions of photons is shown up to having 7 total photons in 2 modes. Because of the much simpler photon distribution term when only 2 modes are present in the system, it may be possible to find a modal spectral distribution which has an analytically exact result that could verify the algorithm, but none were found thus far.

Table 4.2 Photon distribution table for two modes and photon numbers between 1 and 7. Some patterns emerge like the Kronecker Delta multiplied by the photon number for the first two distributions.

	***n* = 1**		***n* = 2**		***n* = 3**		***n* = 4**		***n* = 5**		***n* = 6**		***n* = 7**	
***d* = 1**	1	0	2	0	3	0	4	0	5	0	6	0	7	0
***d* = 2**	0	1	0	2	0	3	0	4	0	5	0	6	0	7
***d* = 3**	-	-	1	1	2	1	3	1	4	1	5	1	6	1
***d* = 4**	-	-	-	-	1	2	1	3	1	4	1	5	1	6
***d* = 5**	-	-	-	-	-	-	2	2	3	2	4	2	5	2
***d* = 6**	-	-	-	-	-	-	-	-	2	3	2	4	2	5
***d* = 7**	-	-	-	-	-	-	-	-	-	-	3	3	4	3
***d* = 8**	-	-	-	-	-	-	-	-	-	-	-	-	3	4

$$n_{m,d} = \sum_{a=0}^{\frac{n-1}{2}} (n-2a)\delta_{m,d-2a} + \sum_{a=0}^{\frac{n-2}{2}} (a+1)\delta_{2a+3,d} + \sum_{a=0}^{\frac{n-3}{2}} (a+1)\delta_{2a+4,d} \tag{4.3.2}$$

Substituting equation (4.3.2) into the probability density function (4.1.6), using (4.2.4) as the modal distribution, and setting the number of modes to 2 results in an exact solution for the photon probability density function of having any arbitrarily large number of photons. This process allows for any order approximations to be used in the previously described algorithm, where the order refers to the number of terms, or photons in this case, in the probability expansion of $P(n)$. The higher order approximations will still only be exact for an average photon number of 0, but will be in general more accurate for non-zero average photon numbers as seen in Figure 4.4.

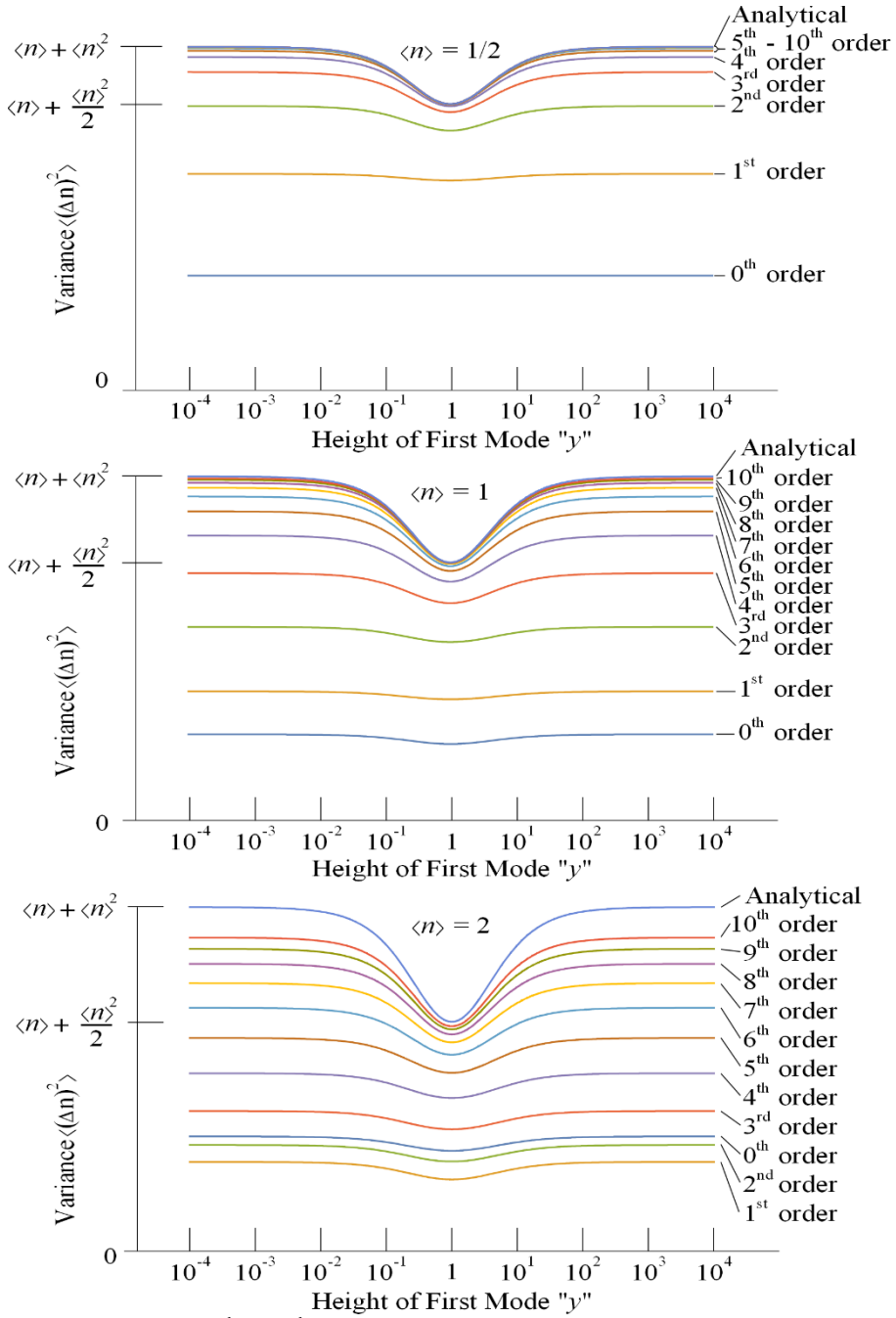

Figure 4.4 Photon statistics for 0^{th} to 10^{th} order approximations for 2 modes as depicted in Figure 4.1B. (Top) Average photon number equal to 0.5, as the order of the approximation increases, the variance is more accurate. (Middle) Average photon number equal to 1. (Bottom) Average photon number equal to 2, 10^{th} order approximation is already not enough to accurately estimate the variance. Also notice that the 1^{st} and 2^{nd} order approximations are less accurate than the 0^{th} order.

To determine if the analytical results obtained thus far are correct to any arbitrarily high number of average photons, the algorithm can be used with higher order approximations to the variance. Plugging in the higher order approximations into the algorithm before the normalization step results in the exact same analytical result as equation (4.2.12) up to the 10^{th} order approximation. This strongly suggests but does not prove the analytical results obtained thus far with the first order approximation as well as the algorithm are correct.

It should be noted that the 0^{th} order approximation does not produce the same result as the other approximations and the first order is the simplest and fastest to implement that gives the correct result.

For any of the approximations to be accurate within 1ppm it was found that the order of the approximation needs to be about 20 times the average photon number when the average photon number is greater than 1. This means that the 10^{th} order approximation is accurate for average photon numbers less than 1/2. Taking the 1000^{th} order approximation with an average photon number of 1 produces a result that is accurate out to 395 decimal places. Also the approximation did not exceed the analytical result; given that the variance is a sum of positive numbers the approximation must always be less than and converge to the analytical result if the analytical result is correct.

Because the higher order approximations are only useful without an analytical result they will no longer be used in this Chapter and only the first order will be used in the algorithm.

4.4 Lorentzian and Gaussian Spectral Distributions

Thus far we have established a method for obtaining the variance of a thermal source of photons accurate for any expected photon number, but only for a certain distribution. This method can be expanded to cover many different modal spectral distributions. Lorentzian and Gaussian peaks are common in spectral distributions and can be seen in Figure 4.5 and will be discussed next.

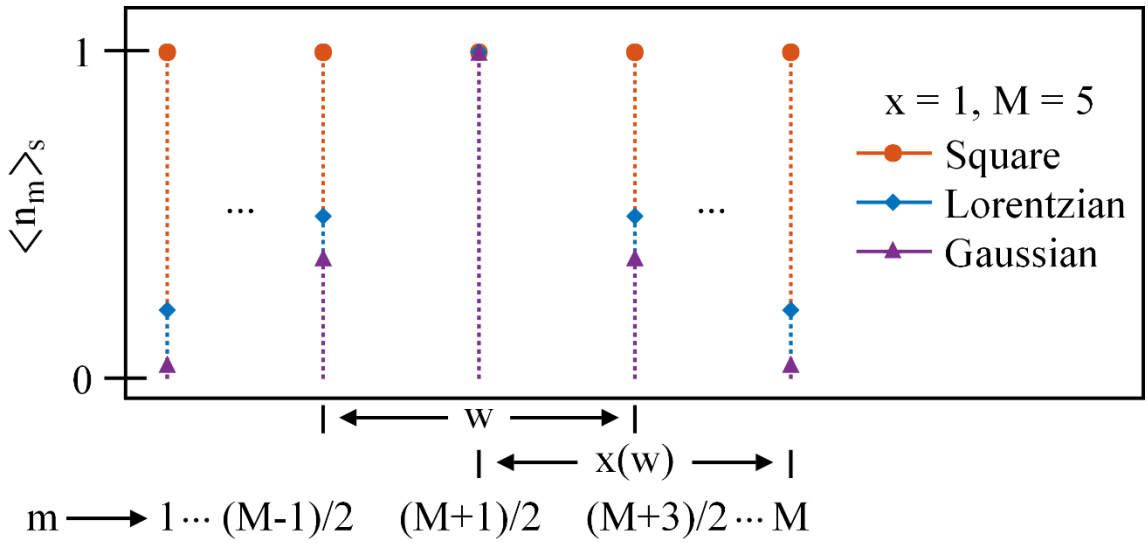

Figure 4.5 Square, Lorentzian, and Gaussian spectral mode distributions, where x is the peak width multiplier. The Lorentzian and Gaussian curves will only be studied for an odd number of modes, even number of modes work but have different properties as none of the modes would be centered at the peak.

The average photon number before normalization for the Lorentzian and Gaussian distributions are defined by the following equations with the subscripts *L* and *G* respectively. In the following equations the number of modes, *M*, is limited to only the odd integers, and *x* represents the width of the spectral peak. When $x = 0$ the spectrum would be uniform because all of the modes would be located at the center of the peak, when $x = 1$ the side modes exist within 1 width of the peak on each side, and when $x \to \infty$

the spectrum would be single mode because only one mode would be at the center of the peak, and the side modes would have 0 average photon numbers.

$$\langle n_m \rangle_L = \frac{1}{1 + \frac{4(1-2m+M)^2 x^2}{(M-1)^2}} \tag{4.4.1}$$

$$\langle n_m \rangle_G = exp\left[\frac{-4(1-2m+M)^2 x^2}{(M-1)^2}\right] \tag{4.4.2}$$

In the first step of normalizing the mode distribution the Gaussian curve already causes problems in that there is no solution to the finite sum of a Gaussian. The Lorentzian can be normalized but will cause problems latter in the algorithm. The issue for both curves is that the number of modes is a variable. Focusing on just 3 or 5 modes allow for all the difficulties of indeterminate sums to be ignored and the normalized spectral modes are given below.

$$\overline{\langle n_m \rangle_L|_{M=3}} = \frac{\langle n \rangle (1 + 4x^2)}{(3 + 4x^2)(1 + 4(m-2)^2 x^2)} \tag{4.4.3}$$

$$\overline{\langle n_m \rangle_L|_{M=5}} = \frac{\langle n \rangle (1 + 5x^2 + 4x^4)}{(5 + 15x^2 + 4x^4)(1 + (m-3)^2 x^2)} \tag{4.4.4}$$

$$\overline{\langle n_m \rangle_G|_{M=3}} = \frac{\langle n \rangle e^{-4(m-3)(m-1)x^2}}{2 + e^{4x^2}} \tag{4.4.5}$$

$$\overline{\langle n_m \rangle_G|_{M=5}} = \frac{\langle n \rangle e^{-(m-5)(m-1)x^2}}{2 + e^{3x^2}\left(2 + e^{x^2}\right)} \tag{4.4.6}$$

Finding the probabilities of having 0 or 1 photon for the Lorentzian and Gaussian distributions follows easily from the previous spectrums analyzed but the resulting equations are long and complex and therefore will not be written out specifically until the

final solution. After finding the probabilities and pre-normalized variance the normalization step can be simplified. It is known that the variance, for any spectral distribution, should be within the limits of single mode and infinite modes so that the normalized variance can be reduced to $\overline{\langle(\Delta n)^2\rangle} = (\langle(\Delta n)^2\rangle - \langle n\rangle)/\langle n\rangle^2$ and the de-normalization is simplified to $\langle(\Delta n)^2\rangle = \langle n\rangle + \langle n\rangle^2\overline{\langle(\Delta n)^2\rangle}$. These equations are found by setting M_1=1 and finding the limit of equations (4.2.9) and (4.2.11) as $M_0 \to \infty$.

After finding the limit of the normalized variance as the average photon number goes to zero and de-normalizing, the final result is obtained for Lorentzian and Gaussian modal distributions as seen in the following equations.

$$\langle(\Delta n)^2\rangle_L|_{M=3} = \langle n\rangle + \langle n\rangle^2 \frac{(3 + 8x^2 + 16x^4)}{(3 + 4x^2)^2} \tag{4.4.7}$$

$$\langle(\Delta n)^2\rangle_L|_{M=5} = \langle n\rangle + \langle n\rangle^2 \frac{(5 + 30x^2 + 67x^4 + 40x^6 + 16x^8)}{(5 + 15x^2 + 4x^4)^2} \tag{4.4.8}$$

$$\langle(\Delta n)^2\rangle_G|_{M=3} = \langle n\rangle + \langle n\rangle^2 \frac{\left(2 + e^{8x^2}\right)}{\left(2 + e^{4x^2}\right)^2} \tag{4.4.9}$$

$$\langle(\Delta n)^2\rangle_G|_{M=5} = \langle n\rangle + \langle n\rangle^2 \frac{\left(2 + 2e^{6x^2} + e^{8x^2}\right)}{\left(2 + 2e^{3x^2} + e^{4x^2}\right)^2} \tag{4.4.10}$$

The results from equations (4.4.7) through (4.4.10) can be seen in Figure 4.6. As expected, the variance calculated from a Gaussian distribution is slightly larger than for the Lorentzian distribution. This is due to the Gaussian quickly decaying to 0 away from the peak whereas the Lorentzian slowly approaches 0. Because of this the side modes in

the Gaussian distribution are slightly smaller, meaning the distribution is a closer approximation to a single mode where the variance is maximized.

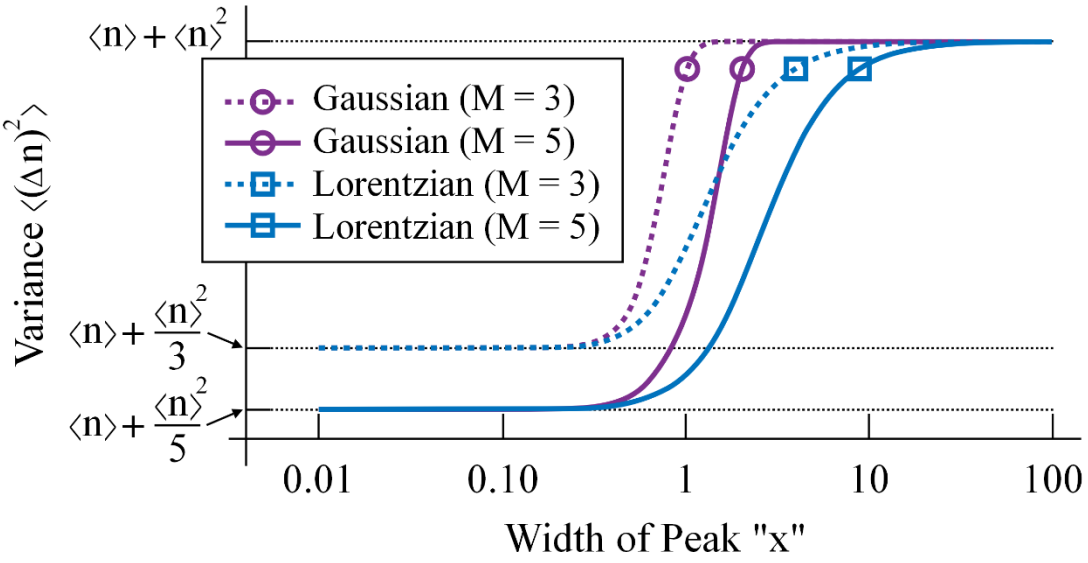

Figure 4.6 Comparison of the variance in Gaussian and Lorentzian spectral distributions. At small values of *x* the distribution in both cases is approximately a square distribution and the result reduces to the standard form given in equation (4.1.13). When *x* is large, the side modes are very small and the distribution is approximately a single mode.

From Figure 4.6 it can be seen that the variance from a Gaussian distribution with more modes can surpass that of a Lorentzian with fewer modes. The variance calculated from the Gaussian distribution with 5 modes is greater than the variance from a Lorentzian distribution with 3 modes for *x* greater than 1.53.

4.5 Design of Thermal Photon Noise Dependent Devices

Up until now thermal photon noise has been talked about theoretically rather than based on spectra from actual devices. A device that may produce thermal photon noise with a small number of populated modes, is a microcavity Fabry-Pérot etalon with an absorbing material within the cavity.

A Fabry-Pérot etalon is an optical device depicted in Figure 4.7 where a plane wave with the correct frequency is coupled into a cavity between two reflecting mirrors as long as the first mirror has a reflectance less than unity. If there exists an absorbing media in the cavity only certain frequencies of light will couple into the cavity and absorb, significantly limiting the number of possible absorption modes. Following Kirchhoff's law these same modes are the only allowed thermal emission modes if the cavity is heated.

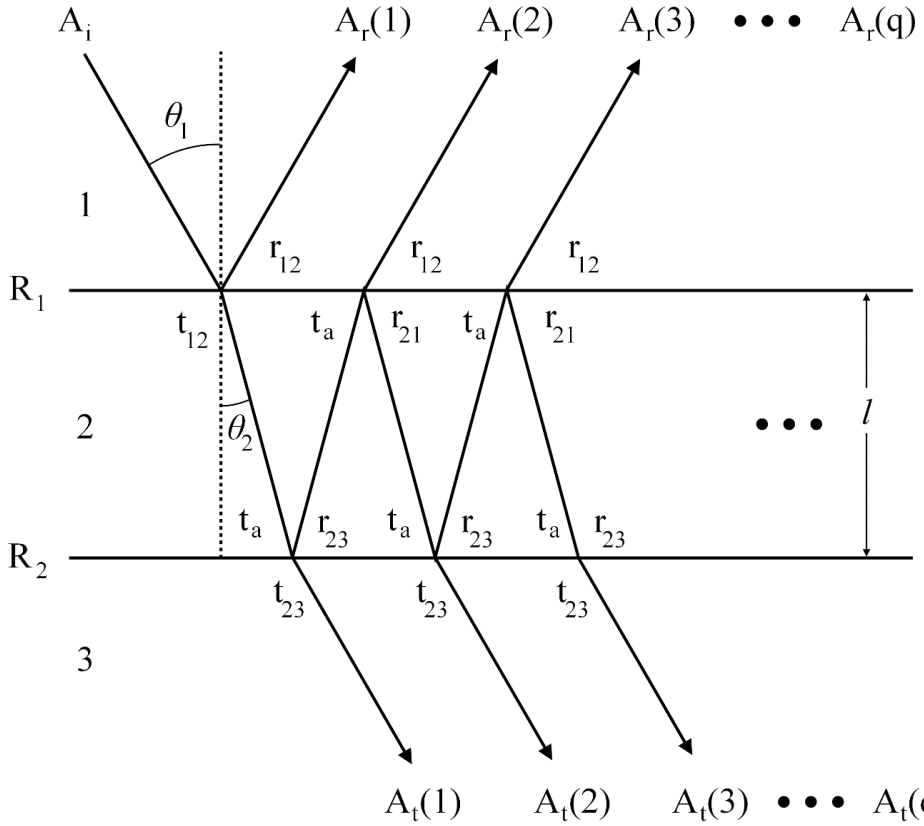

Figure 4.7 Fabry-Pérot etalon. A_i is the complex amplitude of the incoming plane wave at angle θ_1, each A_r and A_t is the complex amplitude of the reflected and transmitted wave respectively, R_1 and R_2 are the intensity reflection coefficients of the first and second mirror respectively, r_{xy} and t_{xy} is the complex reflectivity and transmission going from material x to y (e.g. $r_{12} = -\sqrt{R_1}$ and $t_{12} = \sqrt{1 - R_1}$), t_a is the single pass complex transmission through the cavity.

To find the total reflection, transmission, and absorption coefficients for the Fabry-Pérot etalon an infinite sum of the complex waves reflected and transmitted is computed as in the following equations [62].

$$A_r = r_{12}t_{12}t_{21}\sum_{q=2}^{\infty} t_a^{2(q-1)} r_{21}^{(q-2)} r_{23}^{(q-1)} e^{i(q-1)\phi}$$

$$A_r = r_{12} + \frac{e^{i\phi} r_{23} t_{12} t_{21} t_a^2}{1 - e^{i\delta} r_{21} r_{23} t_a^2} \tag{4.5.1}$$

$$A_t = t_{12}t_{23}\sum_{q=1}^{\infty} t_a^{(2q-1)} r_{21}^{(q-1)} r_{23}^{(q-1)} e^{i(q-1)\phi}$$

$$A_t = \frac{t_{12} t_{23} t_a}{1 - e^{i\phi} r_{21} r_{23} t_a^2} \tag{4.5.2}$$

$$\mathbb{R} = A_r A_r^* \tag{4.5.3}$$

$$\mathbb{T} = A_t A_t^* \tag{4.5.4}$$

$$\mathbb{A} = 1 - \mathbb{R} - \mathbb{T} \tag{4.5.5}$$

In the previous equations the round trip phase delay in the cavity, ϕ, is defined as $\phi = 4\pi n_2 l \cos(\theta_2)/\lambda$. Equation (4.5.5) represents the spectroscopic absorptivity or emissivity of the cavity. For thermal emission the emissivity multiplied by the average energy of photons in a mode predicted by Planck's law, as given in the explanation of equation (4.1.3), will produce an actual modal spectral distribution as seen in Figure 4.8.

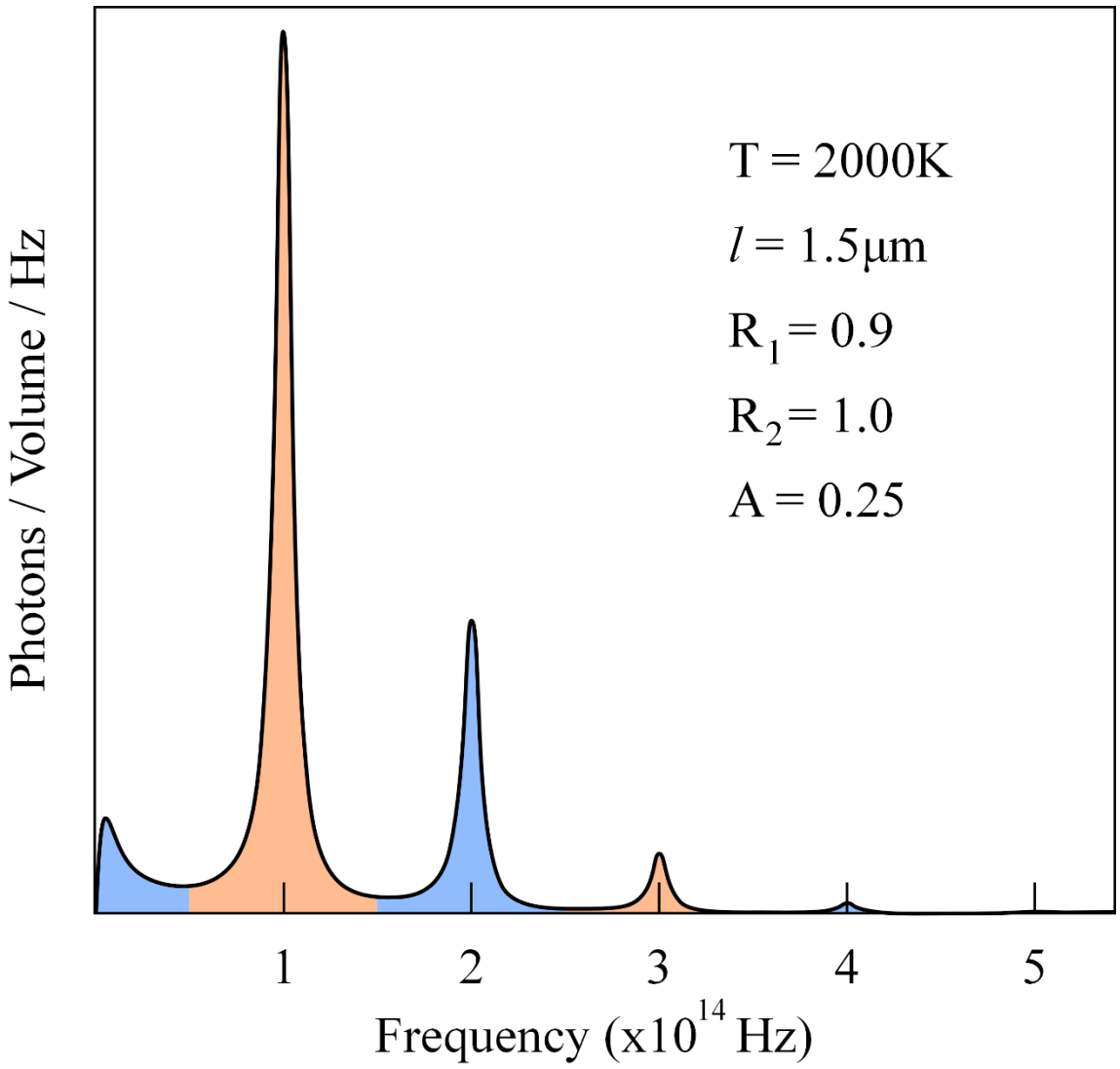

Figure 4.8 Modal spectral distribution of a thermal source at 2000K in a microcavity. The mode spectrum is decidedly non-uniform. Each mode in the cavity is highlighted to show the integration bounds

A useful parameter for the spacing of the modes can be calculated from the round trip phase delay as seen in equation

$$\Delta\nu = \frac{c}{2n_2 l\cos(\theta_2)} \tag{4.5.6}$$

It can then be shown that the number of modes in a microcavity are governed by the following equation.

$$N = \frac{8\pi v^2 n_2^3 V}{c^3} dv \tag{4.5.7}$$

In the previous equation v is the frequency of light, dv is the width of the mode and is approximated by the full width half maximum of the mode, c is the speed of light, and V is the volume of the cavity. The full width half maximum of the modes can be determined by the following equation, by setting the denominator equal to 2 times the numerator of equation (4.5.4), as done in Yariv [62].

$$\Delta\nu_{1/2} = \frac{c\left(1-(1-A)\sqrt{R_1 R_2}\right)}{2\pi n_2 l \cos(\theta_2)\,(1-A)(R_1 R_2)^{\frac{1}{4}}} \tag{4.5.8}$$

Typically equation (4.5.8) is seen with a single pass absorption, A, of 0 and the reflectivity of the two mirrors equal to R. Using equation (4.5.8) and (4.5.7) an estimate of the number of modes in a cavity can be found. If a cavity design with a first order mode at 3μm = 10^{14}Hz, a dv of 10^{13}Hz (A = 0.25, R_1 = 0.9, R_2 = 1.0, n_2 = 1, l = 1.5, θ_2 = 0), and a volume equal to the wavelength cubed, the number of modes is approximately 2.5. It is very possible to increase the first mirror reflectivity and decrease the single pass absorption to predict exactly 1 mode per spectral peak in Figure 4.8.

Integrating over the each individual mode in Figure 4.8 and multiplying by the volume of the cavity results in a unique modal spectral distribution defined in the following table. The volume of this cavity was defined as $V = l * \lambda^2 = 13.5\ [\mu m^3]$.

Table 4.3 Modal spectral distribution for thermal photons in a Fabry-Pérot cavity with a thermal source at 2000K. For higher order modes the number of photons is small such that the cumulative sum of photons in all modes is about equal to the sum of the first 7 modes.

Mode Index (m)	Number of Photons ($\langle n_m \rangle$)
0	0.017
1	0.11
2	0.037
3	0.0077
4	0.0012
5	0.00018
6	0.000023

Using the spectrum developed above and presented in Figure 4.8 and Table 4.3 the variance calculated using the first order approximation algorithm is shown to be.

$$\langle (\Delta n)^2 \rangle \cong \langle n \rangle + .459 \langle n \rangle^2 \tag{4.5.9}$$

Where the average photon number is known because we can integrate the curve in Figure 4.8 to get the following.

$$\langle n \rangle \cong .173123 \tag{4.5.10}$$

$$\langle (\Delta n)^2 \rangle \cong .186884 \tag{4.5.11}$$

Using the standard equation (4.1.13) in this case would have resulted in a significant difference. The estimation would have resulted in using 2.5 for the number of modes with an error of 12.8% in the B-E term for a total error of about 1% in the variance calculation.

In practice a Fabry-Pérot cavity will be designed with Distributed Bragg Reflectors (DBR's) to provide a tuned reflectivity that can be optimally coupled to the absorptivity of the cavity. These mirrors will not be infinitely thin and introduce their own phase delay into the system. Furthermore an absorbing plate such as a bolometer will provide another index change where the light can reflect from and introduce another phase delay. If the absorbing layer is kept thin enough such that the wave is minimally perturbed then the above equation will still work for estimates of the first order mode defined as the first have wave $\lambda \cong 2nl$. Higher order modes of larger integer half waves will not be estimated very accurately because the DBR mirrors will have a significantly different reflectivity for different frequency light.

4.6 Detecting Thermal Photon Noise

The above Fabry-Pérot design accomplishes the goal of absorbing thermal photons, and will be used to detect small changes in thermal photon noise. To be able to detect thermal photons noise the uncertainty in absorber position must not be limited by vibrations due to thermal-mechanical motion. The motion of a mechanical structure can be shown to follow the equation below due to thermal variations in the system [63].

$$\sqrt{\langle (\Delta z)^2 \rangle_{TM}} \cong \sqrt{\frac{k_B T}{k}} \tag{4.6.1}$$

In the previous equation the thermal-mechanical noise is estimated from the classical equipartition theorem, which states that there is $\frac{1}{2} k_B T$ energy in each mechanical degree of freedom, and *k* is the spring constant of the system. In the case of

the bolometer clamped at the edges it was assumed to vibrate in the first order mode, the vertical, z-direction; whereby the energy is stored in the spring such that $\frac{1}{2}k_BT = \frac{1}{2}kz^2$. Note that the other directions also have $\frac{1}{2}k_BT$ of energy but the spring constant in those directions is much larger and horizontal variations do not affect the properties of the cavity. The spring constant of the bolometer can be calculated for a membrane, attached at all sides like a stretched drum, by assuming the membrane is thin and has an internal biaxial tensile stress of σ [64].

$$k \cong \frac{\pi^2 \sigma H}{16 * .47} \tag{4.6.2}$$

In the previous equation *H* is the thickness of the bolometer and will be 25nm in the design later, and a typical internal stress is 300MPa for Micro-Electrical Mechanical Systems (MEMS) thin films, giving a spring constant of about 10N/m. This results in a total integrated thermomechanical noise of about 52pm in the z direction for a source at 2000K given in Figure 4.8. If a more conservative estimate is used where the membrane is held up with long thin legs to thermally isolate the bolometer from the surroundings as in [22,26,27], the spring constant would be on the order of 1000 times less, and operating at room temperature, resulting in a thermomechanical noise of 650pm.

Photon counting noise will then cause an additional noise term due to a limited number of photons being present in the cavity. This noise does not come from the photon pressure as these devices will have very few photons; so few in fact that the photons do not move the plate any measurable amount. Caves and Edelstein [65,66] have formulated

the photon counting statistics for predicting the uncertainty in position produced from having a limited number of photons by the following equation.

$$\langle(\Delta z)^2\rangle_{PC} \cong \left(\frac{\lambda}{4\pi F}\right)^2 \frac{1}{\langle(\Delta n)^2\rangle} \tag{4.6.3}$$

In the previous equation F is defined as the finesse of the cavity and is sometimes quoted as the number of internal reflections a photon undergoes in the cavity. For a Fabry-Pérot with an absorbing cavity the finesse is given by the following.

$$F = \frac{\Delta\nu}{\Delta\nu_{1/2}} = \frac{\pi\sqrt{(1-A)\sqrt{R_1R_2}}}{\left(1-(1-A)\sqrt{R_1R_2}\right)} \tag{4.6.4}$$

Combining equations (4.6.3) and (4.6.4) the final term for the photon counting noise term is given by,

$$\langle(\Delta z)^2\rangle_{PC} \cong \left(\frac{\lambda}{4\pi}\right)^2 \frac{\left(1-(1-A)\sqrt{R_1R_2}\right)^2}{\pi^2(1-A)\sqrt{R_1R_2}} \frac{1}{\langle(\Delta n)^2\rangle} \tag{4.6.5}$$

Calculating the photon counting noise for the cavity studied earlier for 3μm light using the corrected variance in (4.5.11) gives a noise of ~60nm. This is a large positional uncertainty with $\langle n\rangle \sim 0.17$, $\langle(\Delta n)^2\rangle \sim 0.19$, and $F \sim 9.19$. Using the estimated variance with 2.5 modes would only show a 0.5% difference in the calculation. Using only Poissonian statistics as was used in the references would result in a 4% error. However, the important feature here is that 60nm is much larger than the thermomechanical noise and these effects should be seen in a small subset of cases. In order for the photon counting noise to overwhelm the thermomechanical noise the system must be photon starved, meaning the number of photons must be small. Conversely the number of

photons needs to be large enough that errors from the spectral mode distribution in the B-E term of the variance carry through to errors in the total variance estimated solely from Poissonian statistics. It should be noted that if the average number of photons is small enough to neglect the B-E variance term the detection or minimization of photon counting noise is still an important problem for high finesse microcavities. Figures 4.9 and 4.10 shows the dichotomy between these two effects on the positional noise of the bolometer membrane.

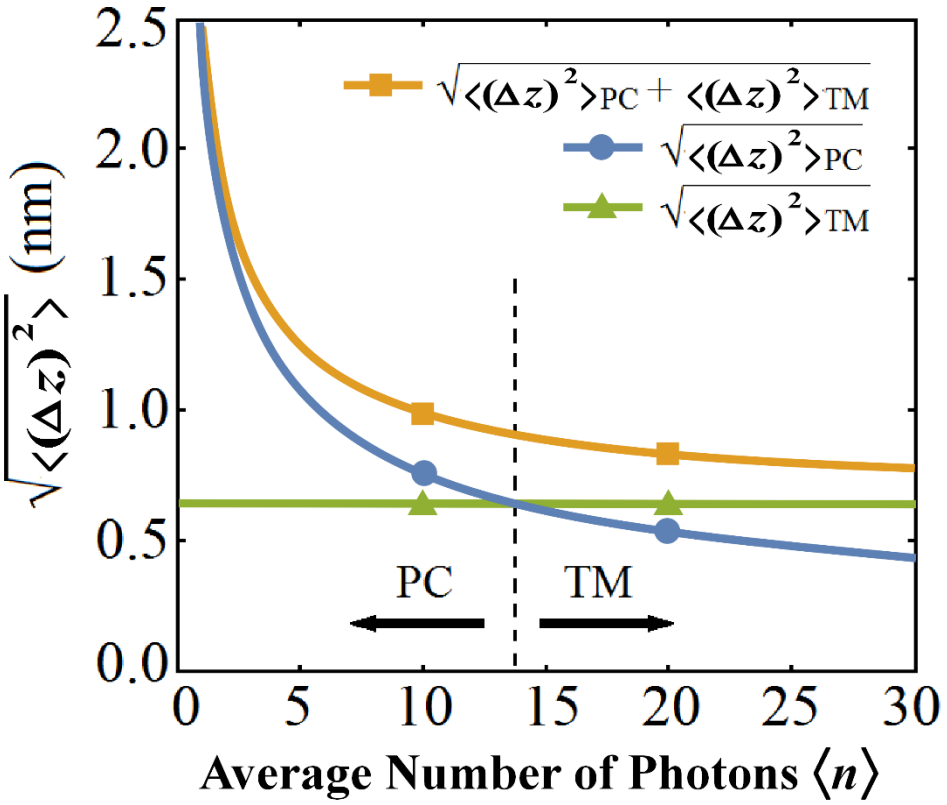

Figure 4.9 Photon counting and thermomechanical noise for a micro-bolometer assuming Poissonian statistics only. If the $\langle n \rangle^2$ term is included in the variance the photon counting noise term would decay to 0 much faster as the average number of photons increases. This is because the photon counting noise is inversely proportional to the variance.

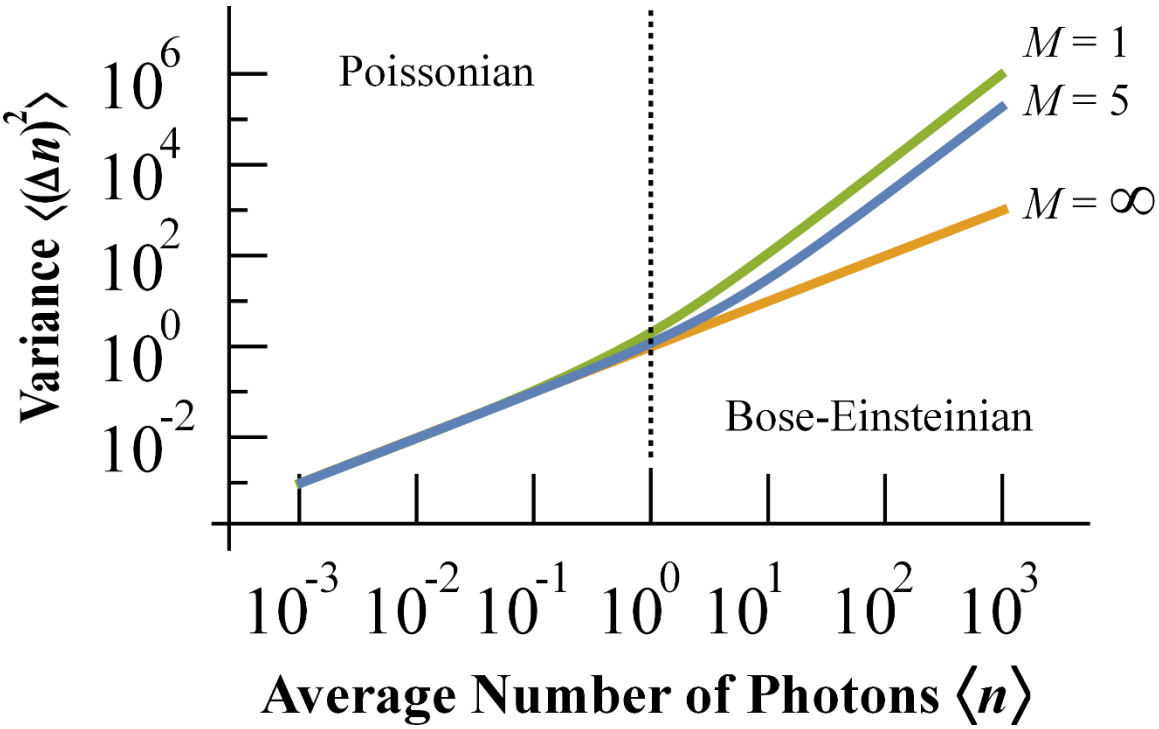

Figure 4.10 Variance of thermal photons determined by the standard equation given in (4.1.13). Having a large average number of photons is required to see a difference in the variances for different cavities.

The dichotomy between maximizing photon counting noise and maximizing the B-E contribution to the thermal photon noise provides some interesting design guidelines. For instance, if a photon noise detector is needed such that a difference in variance of 0.01nm in the vertical direction is discernable then a cavity is needed that is very dependent on the placement of the absorber within the cavity. This can be accomplished with the design in Figure 4.11, where un-doped Ge and SrF_2 are used for the DBR mirrors, and doped Ge is used for the absorber resulting in a cavity with a peak absorption at 3μm and a Finesse of about 59.1. The design was simulated using the matrix method for optical layered media developed in Pochi Yeh's book [67].

Figure 4.11 Layer structure for a Fabry-Pérot cavity with a design wavelength of 3μm and a Finesse of 59.1. This structure gives a peak absorption of 99.4% at 3.001μm. Note that the illustration is not to scale.

When the doped Ge absorber vibrates within the cavity to the extent predicted by photon counting and thermomechanical noise the center frequency as well as the peak

absorption value. For this design it was desired to have a large change in the center frequency of the peak in order to detect small changes in the variance of the noise. It can be seen in Figure 4.12 that for small changes in absorber position the center wavelength linearly changes at about a 1:1 ratio. The linearity actually remains accurate to within a few percent for changes in vertical position as large as the cavity. This means for a spectrometer with a resolution of $1cm^{-1}$ a change in center frequency of 0.9pm is detectable at a wavelength of 3μm, allowing for variations as small as 0.9pm in the vertical position to be resolvable. The thermomechanical noise can be much larger than this so techniques would have to be introduced to limit the thermomechanical noise further. Although the spectrometer would be able to detect this small change it would also have to either be fast enough to see the changes in real time or be able to measure absorption peak broadening with a longer integration time as seen later in Figure 4.14.

To measure the photon counting statistics in real time the spectrometer needs to have an integration time on the order of how long a photon lasts in the cavity, as long as that time is either much less than the inverse of the resonant frequency of the thermomechanical noise as in equation (4.6.6) or the thermomechanical noise is much smaller than the photon counting noise. A photon will reflect from the mirrors about as many times as the finesse of the cavity.

$$\tau < \tau_{PC} = \frac{Fl}{c} < \tau_{TM} = \sqrt{\frac{m}{k}} \tag{4.6.6}$$

In equation (4.6.6) for the cavity designs thus far the spectrometer would need an integration time on the order of 0.5ps, much too fast to see the photon noise with a

spectrometer or even a photodetector in real time. In this case the thermomechanical noise is both smaller and much slower at a time constant of about 1μs. For a cavity with a very large finesse and cavity length then the time constant could be large enough to detect small differences in thermal photon noise. Remembering if the cavity is large then the volume will increase and the number of photons in the cavity will increase, reducing the mechanical response to photon counting noise, and the thermomechanical noise may start to dominate the noise mechanisms. In this case a different membrane with a higher vertical spring constant can be used to reduce the thermomechanical noise.

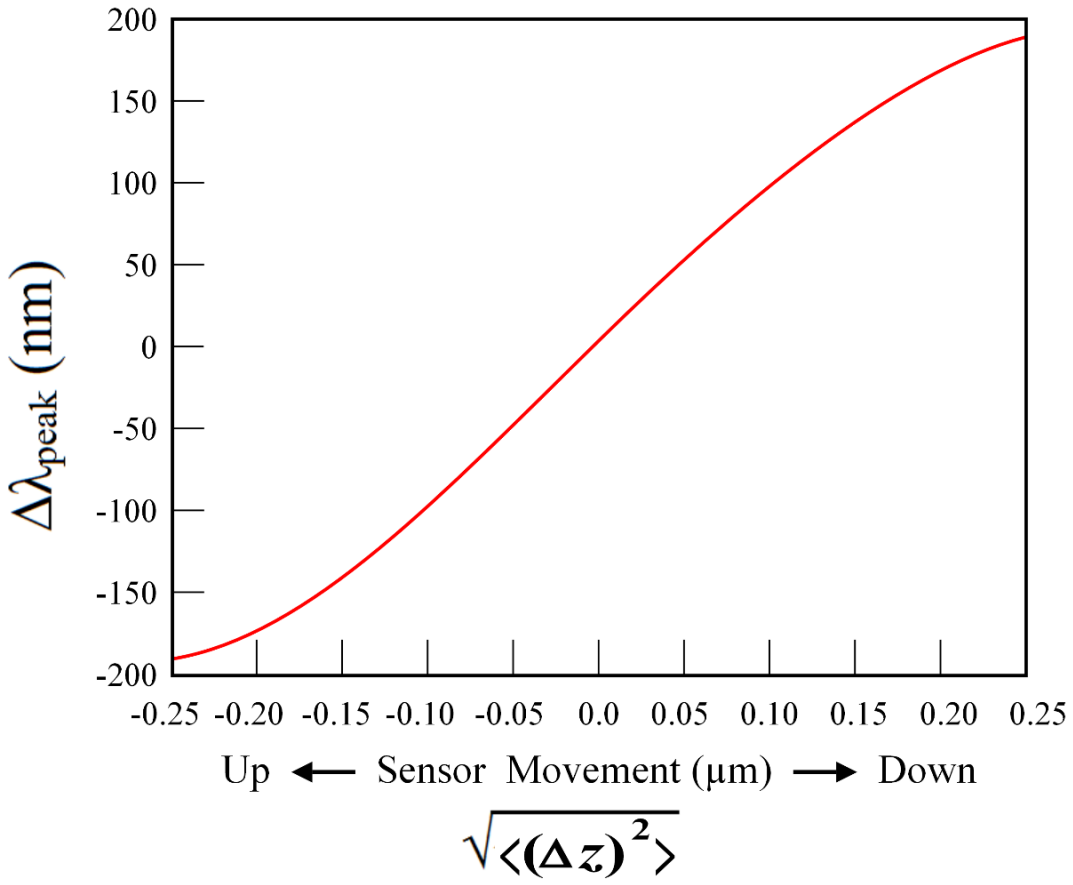

Figure 4.12 Spectral response of bolometer movement within a cavity.

With about 1pm of mechanical resolution could this cavity design (with a cavity size of *C(l)*, where *C* is a large integer, to increase the minimum integration time) detect the small changes in spectrally dependent photon variance? To find the solution the square root of mechanical variance due to photon counting noise (4.6.5) is taken and the partial derivative is computed of the noise with respect to thermal photon variance. Then the change in photon variance is solved for, resulting in an equation that relates the detectable mechanical noise to the detectable photon noise as shown in equation (4.6.7).

$$\sqrt{\langle(\Delta z)^2\rangle_{PC}} = \sigma_z$$

$$\sqrt{\langle(\Delta n)^2\rangle} = \sigma_n \tag{4.6.7}$$

$$d\sigma_n = -\left(\frac{4\pi F}{\lambda}\right)(d\sigma_z)(\sigma_n)^3$$

Plugging in for an F of 59.1, λ of 3μm, $d\sigma_z$ of -1pm, and σ_n from equation (4.5.11) gives a change of about 10^{-6} photons are detectable. That means it would be easy to detect the 1% change in variance predicted by the spectrally dependent thermal photon noise model.

In the case of a high finesse cavity that would be used to selectively detect thermal radiation in a narrow spectral window it would be undesirable to have such a high amount of uncertainty in the center frequency due to the photon-counting or thermomechanical noise. A large uncertainty in center frequency would essentially lead to spectral line width broadening, ultimately limiting the spectral resolution of the device, due to the measurement being averaged over many photon interactions.

In this case a simple design change is needed where a layer of Ge is added before the first layer after the cavity in Figure 4.11, and the cavity size increased significantly so that it is about a half wave thick rather than a quarter wave. With the absorbing layer the thickness of the cavity was not determined analytically, rather it was simulated for many cavity sizes and optimized for the largest absorption at the center frequency. For the new design the thickness of the air gap on each side of the absorber was set to 555nm. The spectral response of the two designs can be seen in Figure 4.13. The new design will have a peak absorption of 83.6 at 2.995μm with a finesse of 41.2.

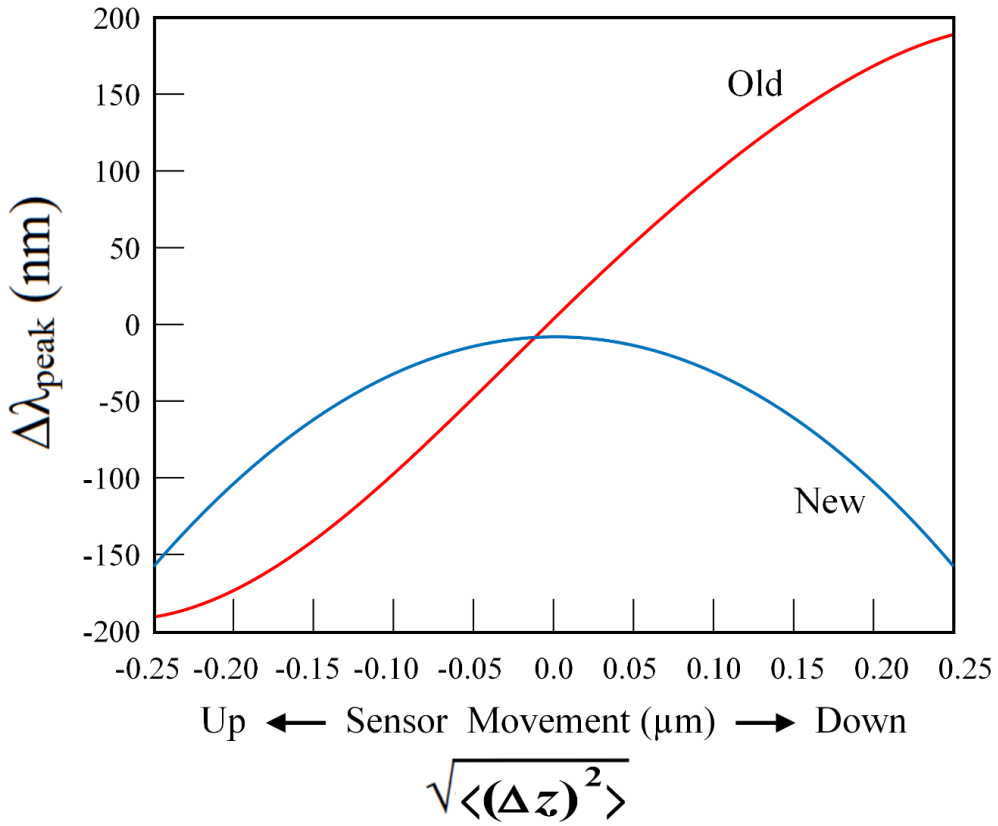

Figure 4.13 Spectral response for the New and Old cavity designs. The new design has a flat region when the absorber is in the middle of the cavity resulting in relatively little change in the center frequency for small vibrations.

In Figure 4.13 it can be seen that the center frequency has relatively little change when the mechanical vibrations are small. In the first 50nm of movement up or down the center frequency only shifts 7nm, much less than the 100nm of shift in the first design. If the spectral responses of the two cavities are averaged over the range of mechanical vibrations then the actual spectral response with photon counting noise broadening can be found as in Figure 4.14.

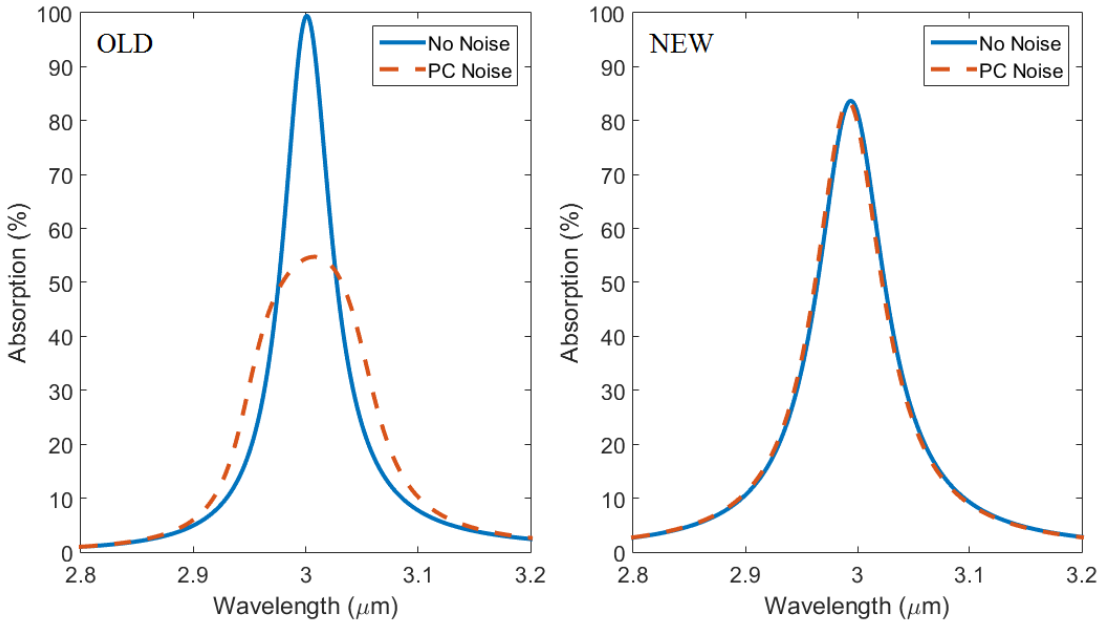

Figure 4.14 Photon counting noise limited peak broadening for two cavity designs. The solid lines were calculated for no noise in the system and the dashed lines are calculated from having 50nm of vertical mechanical noise in the system. (OLD) The first cavity design showing a dramatic reduction in Finesse as well as peak height. (NEW) The second design where the broadened peak is almost indistinguishable from the peak with no noise broadening.

From Figure 4.14 it can be seen that the old and new designs differ greatly in spectral response when photon counting noise is taken into account. In the first design the finesse of the cavity is reduced from 59.1 to 25.4 with photon counting noise broadening. The second design when compared to the first without noise is considered to have a lower

quality (i.e. $F_{OLD} = 59.1 > F_{NEW} = 41.2$) and lower peak absorption, but after factoring in the photon counting noise broadening the new design is much higher quality ($F_{NEW\text{-}Broadened} = 40.9 > F_{OLD\text{-}Broadened} = 25.4$) and has a higher peak absorption ($A_{NEW\text{-}Peak} = 83.42 > A_{OLD\text{-}Peak} = 54.75$).

It would be desirable to have a higher absorption peak in the second design but is difficult to do in practice. As the absorbing plate in the cavity becomes more perfectly coupled to the cavity as in the first design the spectral shift due to mechanical noise becomes more prominent. This is because the small reflections at the interfaces of the absorber get perfectly coupled with the reflections at the mirrors. Any small deviation throws off the phase relation and a different frequency couples into the cavity more efficiently.

One method to combat this issue may be to design the DBR mirrors for slightly off resonance peak reflectivity, for just the top or bottom mirror. This might allow the phase relationship between all the interfaces to be slightly fuzzy and allow for more mechanical variations without sacrificing finesse. This is quite a complex optimization problem that was not tackled here. Instead 2 designs were shown to have significantly different properties relative to the spectral response of mechanical vibrations where both have applicable uses in different applications.

Chapter 5

Conclusion and Future Work

5.1 Laser Heating and Damage

We presented and confirmed an analytical and numerical model for the thermal heating of low absorption materials under laser illumination. The model should be correct for thermal time scales and was tested and confirmed by CW laser heating experiments. For CW laser heating the most important results are equations (2.1.8) through (2.1.10), showing that thermal heating is dependent on the inverse of the beam radius of the laser (W/m) when in the long pulse regime. For materials with a high thermal diffusivity, the equilibrium temperature produced by laser heating can be reached in seconds, and for the short pulse regime in milliseconds. When reporting laser damage thresholds of materials

with CW lasers, this work shows that in many cases, the threshold should be reported in terms of the laser power scaled by the inverse of the beam radius rather than in terms of the irradiance of the laser.

It was then showed that using different power ramping conditions the thermal shock on the optic could be minimized. This finding was reproduced in initial testing where longer power ramps on contaminated optics where able to outperform shorter ramp times. This work is in the very early stages of development but show some promising results to get higher power CW operation in dirty environments.

A physical theory for the contamination-induced breakdown of materials under continuous wave laser illumination was then studied and found to be highly dependent on the effective bandgap of the underlying material. The reason for the bandgap dependence appears to be extreme localized heating from the highly absorbing particulates that cause thermal free carriers to be generated, which sets off a runaway process of free carrier absorption and generation. Other processes of carrier generation and thermalization appear to be non-existent at the low intensities required for contamination-induced laser damage but may play a role after the onset of thermal runaway. It has been predicted that the LDT will increase for spot sizes below the thermal diffusion length and for contamination materials that have lower vaporization temperatures. Furthermore the exponential relationship between LDT and band gap should roll off at higher intensities than can be tested at the current time. This is due to other non-linear damage mechanisms starting to also play a role in the overall damage process at high light intensities.

However all of these affects are also dependent on material bandgap, where increasing bandgap always means higher damage thresholds.

Further verification of the contamination-induced damage threshold of materials under CW laser illumination is desired in the future. Introducing contaminant materials with varying evaporation points would be an easy first test for the theory. Varying spot sizes effect on LDT is also predicted by the theory and should be tested further. Next would be to test more materials with varying bandgaps, including non-Oxide materials. Finally with higher power laser advancements the high intensity roll-off of predicted LDT should also be tested, but cannot be completed at this time due to the lasers not being available for testing.

5.2 Thermal Photon Statistics

The spectral dependence on thermal photon noise was studied for small numbers of modes and an algorithm was developed to analytically find the variance. A few select examples where analytically solved for using the algorithm and showed that the results reduced to the well-known equations in simple cases. It is shown that an approximation using the simplified expression for the variance as in Eq. (1) for photon noise is difficult for some modal spectral distributions and the error in the $\langle n \rangle^2$ factor can exceed 35%. For Gaussian modal distributions it is even shown that 5 modes will have the same variance as a Lorentzian distribution with only 3 modes given the correct peak widths.

The algorithm is simply a first order approximation where only the zero and one photon probabilities are calculated. The second through ten photon probability was

computed, and exactly the same analytical results were found, where each also matches numerical techniques out to the 1000^{th} order approximation. The algorithm and analytical results are a significant advancement in thermal photon noise calculations, especially for microcavity detectors where the mode distributions can be decidedly non-uniform.

It was then shown how this theoretical model could be proved in practice by design a Fabry-Pérot cavity to sense thermal photon noise. The method was then used to show how certain high finesse and small microcavities may in fact have significant peak broadening due to thermal photon noise induced positional uncertainties. A Fabry-Pérot design was then presented that combated these issues to the point where the cavities quality was relatively unaffected by 100nm of positional uncertainty in a 1000nm cavity. It was further reasoned that a better cavity that was even less affected by position uncertainty due to photon counting and thermomechanical noise could be possible to build, although the optimization process would be quite difficult and complex and is left for future work.

Bibliography

[1] S. Moradi, S. Kamal, P. Englezos, and S. G. Hatzikiriakos, Nanotechnology **24**, 415302 (2013).

[2] R. Stoian, a Rosenfeld, D. Ashkenasi, I. V Hertel, N. M. Bulgakova, and E. E. B. Campbell, Phys. Rev. Lett. **88**, 097603 (2002).

[3] J. H. Bechtel, J. Appl. Phys. **46**, 1585 (1975).

[4] M. D. Shirk and P. A. Molian, J. Laser Appl. **10**, 18 (1998).

[5] S. Bodea and R. Jeanloz, Inorg. Mater. **94720**, 4688 (1989).

[6] M. Stoneback, Opt. Eng. **52**, 036001 (2013).

[7] Y. Tian, G. Li, B. Q. Yao, and Y. Z. Wang, Appl. Phys. B Lasers Opt. **103**, 107 (2011).

[8] M. Yamada, K. Nambu, Y. Itoh, and K. Yamamoto, J. Appl. Phys. **59**, 1350 (1986).

[9] R. M. Wood, Opt. Laser Technol. **29**, 517 (1998).

[10] M. Lax, J. Appl. Phys. **48**, 3919 (1977).

[11] M. Lax, Appl. Phys. Lett. **33**, 786 (1978).

[12] E. Liarokapis and Y. S. Raptis, J. Appl. Phys. **57**, 5123 (1985).

[13] P. Sprangle, A. Ting, J. Penano, R. Fischer, and B. Hafizi, IEEE J. Quantum Electron. **45**, 138 (2009).

[14] A. Brown, A. Ogloza, L. Taylor, J. Thomas, and J. Talghader, Appl. Opt. **54**, 5216 (2015).

[15] P. C. Reist, *Aerosol Science and Technology* (McGraw-Hill, 1993).

[16] R. S. Shah, J. J. Rey, and A. F. Stewart, in *Laser-Induced Damage Opt. Mater. 2006.* (2006), p. 640305.

[17] B. C. Stuart, M. D. Feit, A. M. Rubenchik, B. W. Shore, and M. D. Perry, Phys. Rev. Lett. **74**, 2248 (1995).

[18] L. Smalakys, G. Batavičiūtė, E. Pupka, and A. Melninkaitis, Appl. Opt. **54**, 2953 (2015).

[19] S. G. Demos, M. D. Feit, and G. Duchateau, in *SPIE Laser Damage* (2014), p. 92370W.

[20] M. Mero, J. Liu, W. Rudolph, D. Ristau, and K. Starke, Phys. Rev. B **71**, 115109 (2005).

[21] M. Planck, Verhandlungen Der Dtsch. Phys. Gesselschaft **2**, 237 (1900).

[22] J. J. Talghader, A. S. Gawarikar, and R. P. Shea, Light Sci. Appl. **1**, e24 (2012).

[23] P. B. Fellgett, J. Opt. Soc. Am. **39**, 970 (1949).

[24] R. C. Jones, J. Opt. Soc. Am. **37**, 879 (1947).

[25] W. B. Lewis, Proc. Phys. Soc. **59**, 34 (1947).

[26] A. S. Gawarikar, R. P. Shea, and J. J. Talghader, IEEE Trans. Electron Devices **60**, 2586 (2013).

[27] A. S. Gawarikar, Spectrally Selective High Detectivity Uncooled Detectors for the Long Wave Infrared, University of Minnesota, 2013.

[28] K. D. Olson, A. Ogloza, J. Thomas, and J. J. Talghader, J. Appl. Phys. **116**, 123106 (2014).

[29] H. B. Fischer, *Mixing in Inland and Coastal Waters* (Academic Press, 1979).

[30] S. A. Socolofsky and G. H. Jirka, *CVEN 489-501: Special Topics in Mixing and Transport Processes in the Environment*, 5th ed. (Texas A&M University, College Station, 2005).

[31] K. D. Olson, A. Brown, A. Ogloza, J. Thomas, and J. J. Talghader, Nat. Photonics (Under Review 2015).

[32] A. Kasugai, K. Sakamoto, K. Takahashi, M. Tsuneoka, T. Kariya, T. Imai, O. Braz, M. Thumm, J. R. Brandon, R. S. Sussman, A. Beale, and D. C. Ballington, Rev. Sci. Instrum. **69**, 2160 (1998).

[33] A. J. Glass and A. H. Guenther, Appl. Opt. **12**, 637 (1973).

[34] W. F. Krupke, M. D. Shinn, J. E. Marion, J. A. Caird, and S. E. Stokowski, J. Opt. Soc. Am. B **3**, 102 (1986).

[35] T. J. Lu and N. a. Fleck, Acta Mater. **46**, 4755 (1998).

[36] R. F. Pierret, *Advanced Semiconductor Fundamentals* (Prentice Hall, 1987).

[37] X. A. Shen, S. C. Jones, and P. Braunlich, Phys. Rev. Lett. **62**, 2711 (1989).

[38] W. L. Smith, Opt. Eng. **17**, 175489 (1978).

[39] N. Bloembergen, IEEE J. Quantum Electron. **10**, 375 (1974).

[40] A. Schmid, P. Kelly, and P. Bräunlich, Phys. Rev. B **16**, 4569 (1977).

[41] Y. P. Varshni, Physica **34**, 149 (1967).

[42] L. B. Glebov, in *SPIE* (2002), pp. 321–331.

[43] T. Apostolova, Opt. Eng. **51**, 121808 (2012).

[44] I. Blech, J. Appl. Phys. **53**, 4202 (1982).

[45] D. a Clugston and P. a Basore, Prog. Photovoltaics Res. Appl. **5**, 229 (1997).

[46] H. Peelaers, E. Kioupakis, and C. G. Van de Walle, Appl. Phys. Lett. **100**, 011914 (2012).

[47] E. D. Palik, Proc Natl Acad Sci USA **2**, 1096 (1991).

[48] A. L. Marshall and F. J. Norton, J. Am. Chem. Soc. **72**, 2166 (1950).

[49] W. E. Ranz and W. R. Marshall, Chem. Eng. Progr **48**, 141 (1952).

[50] V. K. Pustovalov and G. S. Romanov, Int. J. Heat Mass Transf. **28**, 277 (1985).

[51] A. G. Whittaker, Nature **276**, 695 (1978).

[52] C. W. Carr, H. B. Radousky, A. M. Rubenchik, M. D. Feit, and S. G. Demos, Phys. Rev. Lett. **92**, 087401 (2004).

[53] M. E. Frink, J. W. Arenberg, D. W. Mordaunt, S. C. Seitel, M. T. Babb, and E. A. Teppo, Appl. Phys. Lett. **51**, 415 (1987).

[54] Y. Zhao, T. Wang, D. Zhang, S. Fan, J. Shao, and Z. Fan, Appl. Surf. Sci. **239**, 171 (2005).

[55] R. M. O'Connell, Appl. Opt. **31**, 4143 (1992).

[56] R. R. Gattass and E. Mazur, Nat. Photonics **2**, 219 (2008).

[57] A. Salleo, S. T. Taylor, M. C. Martin, W. R. Panero, R. Jeanloz, T. Sands, and F. Y. Génin, Nat. Mater. **2**, 796 (2003).

[58] S. Brawer, Phys. Rev. B **20**, 3422 (1979).

[59] K. D. Olson and J. J. Talghader, Phys. Rev. A (Under Review 2015).

[60] L. Mandel and E. Wolf, *Optical Coherence and Quantum Optics* (Cambridge University Press, 1995).

[61] L. Mandel, Proc. Phys. Soc. **74**, 233 (1959).

[62] A. Yariv and P. Yeh, *Photonics, Optical Electronics in Modern Communications*, 6th ed. (Oxford University Pres, 2007).

[63] P. R. Saulson, Phys. Rev. D **42**, 2437 (1990).

[64] S. D. Senturia, *Microsystem Design* (Kluwer Academic Publishers, 2001).

[65] C. M. Caves, Phys. Rev. Lett. **45**, 75 (1980).

[66] W. A. Edelstein, J. Hough, J. R. Pugh, and W. Martin, J. Phys. E. **11**, 710 (1978).

[67] P. Yeh, *Optical Waves in Layered Media* (Wiley, 2005).